

CHARACTERIZATION OF A LINEAR FIBER-OPTIC COUPLED DETECTOR

By

MATTHEW ROBERT HOERNER

A THESIS PRESENTED TO THE GRADUATE SCHOOL  
OF THE UNIVERSITY OF FLORIDA IN PARTIAL FULFILLMENT  
OF THE REQUIREMENTS FOR THE DEGREE OF  
MASTER OF SCIENCE

UNIVERSITY OF FLORIDA

2012

© 2012 Matthew Robert Hoerner

To my family: my father, mother, and brother. Without your love and support this publication would not have been possible

## ACKNOWLEDGMENTS

I would like to thank my family for their unending love and support. I would also like to especially thank Dr. Hintenlang for his help and direction with regards to this project, along with my committee members, Dr. Bolch and Dr. Rill. Lastly, this thesis would never have been completed without the encouragement and devotion of my colleagues, who I proudly also refer to as friends.

## TABLE OF CONTENTS

	<u>page</u>
ACKNOWLEDGMENTS.....	4
LIST OF TABLES.....	7
LIST OF FIGURES.....	8
ABSTRACT .....	10
CHAPTER	
1 INTRODUCTION AND OBJECTIVES.....	12
Fiber-Optic Coupled Detectors .....	12
Organ Doses in Radiology Examinations.....	13
Objective.....	14
Fiber-Optic Physics.....	15
Linear Detector Feasibility .....	18
Attenuation Effects on Spatial Sensitivity .....	18
Coupling Effects on Spatial Sensitivity .....	21
2 CHARACTERIZATION OF A LINEAR FIBER-OPTIC COUPLED DOSIMETER....	26
Introduction .....	26
Materials and Methods.....	27
Results.....	28
Discussion .....	31
Conclusion .....	32
3 DEVELOPMENT OF A X-RAY/LIGHT CALIBRATION DEVICE.....	44
Introduction .....	44
Materials and Methods.....	45
Results.....	46
Discussion .....	49
Linearity, Reproducibility, and Energy Dependence.....	49
Detector Resolution .....	50
Conclusion .....	51
APPENDIX	
A CODE FOR TABLE 1-1 & 1-2.....	57
B CODE FOR FIGURE 1-11 .....	58

LIST OF REFERENCES ..... 59  
BIOGRAPHICAL SKETCH..... 62

## LIST OF TABLES

<u>Table</u>		<u>page</u>
1-1	Fiber attenuation at locations distal from the coupling surface .....	22
1-2	Fiber attenuation of skew and meridional rays .....	22
2-1	Reproducibility of measurements for 7-cm FOC detector .....	34
2-2	Reproducibility measurements for 15-cm FOC detector .....	34
2-3	Dosimeter sensitivity .....	34

## LIST OF FIGURES

<u>Figure</u>		<u>page</u>
1-1	Schematic illustrating the position of a linear dosimeter. ....	23
1-2	Diagram illustrating the acceptance and transmission cone. ....	24
1-3	Illustration of skew rays internally reflected inside an optical fiber. ....	24
1-4	Relative transmission of light thru the coupling surface. ....	25
2-1	Energy dependence of the dosimeter. ....	35
2-2	Energy dependence of the dosimeter vs. half-value layer. ....	35
2-3	Energy dependence of the dosimeter for 5.6 mm Al. ....	36
2-4	Energy dependence of the dosimeter for 4.83 mm Al. ....	36
2-5	Energy dependence of the dosimeter for 3.86 mm Al. ....	37
2-6	Energy dependence of the dosimeter for 2.9 mm Al. ....	37
2-7	Percent Depth Dose curves of the ion chamber and FOC dosimeter. ....	38
2-8	Linearity of Linear FOC dosimeter. ....	40
2-9	Spatial sensitivity of the 3-cm dosimeter. ....	41
2-10	Spatial sensitivity of the 5-cm dosimeter. ....	41
2-11	Spatial sensitivity of the 7-cm dosimeter. ....	42
2-12	Spatial sensitivity of the 10-cm dosimeter. ....	42
2-13	Spatial sensitivity of the 12-cm dosimeter. ....	43
2-14	Spatial sensitivity of the 15-cm dosimeter. ....	43
3-1	Schematic of x-ray/light field evaluation setup. ....	52
3-2	Plot of detector response to x-ray beam intensity. ....	53
3-3	Detector's response to x-ray beam energy. ....	53
3-4	Comparison of the 3-mm and 42-mm FOC detectors. ....	54
3-5	Detector spatial response perpendicular to the heel effect. ....	54

3-6	Detector spatial response parallel with heel effect.....	55
3-7	The 4.2-cm and 1.5-cm detector's spatial sensitivity. ....	55
3-8	Plot of a detector's theoretical spatial sensitivity response.....	56

Abstract of Thesis Presented to the Graduate School  
of the University of Florida in Partial Fulfillment of the  
Requirements for the Degree of Master of Science

## CHARACTERIZATION OF A LINEAR FIBER-OPTIC COUPLED DETECTOR

By

Matthew Robert Hoerner

May 2012

Chair: David Hintenlang  
Major: Biomedical Engineering

Research in fiber-optic coupled (FOC) x-ray detectors has intensified over the past decade. Fiber-optic detection systems offer many benefits that other instrumentation does not possess, such as minimal angular dependence, real-time measurement capabilities, and small size. Currently at the University of Florida (UF), FOC dosimeters have been used to quantify organ dose measurements in anthropomorphic phantoms irradiated by diagnostic imaging x-ray beams.

The linear FOC detector was adapted from the current point dosimetry system at UF, and evaluated for various dosimetric parameters. After determining that the linear FOC detector was capable of detecting photons independently of sensitive element geometry, the system was also characterized to measure the absorbed dose along the entire sensitive region, improving current methods of quantifying organ doses in radiology.

The application of these systems to other areas of research is still mostly undiscovered. There has been little documented research surrounding linear detectors used as a x-ray-to-light field collimation tool. The development of a device capable of quantifying the x-ray-to-light field alignment would suffice as a convenient alternative to

traditional measurement techniques. The system being investigated provides rapid and accurate evaluation of the spatial difference between x-ray and light fields. An FOC detector element providing a variable output as a function of exposed dosimeter length is used to measure the deviation of each side of the x-ray-to-light field edges.

## CHAPTER 1 INTRODUCTION AND OBJECTIVES

### **Fiber-Optic Coupled Detectors**

The implementation of fiber-optic devices in radiation dosimetry has significantly progressed over the past decade. The basis of fiber optics focuses on the propagation of light through a transmitting medium. This is accomplished by the physical principle known as internal reflection. When applied to dosimetry, the fiber-optic system uses a scintillating material as the light source and a readout device which quantifies the number of light photons that pass through it.<sup>1</sup> The scintillator isotropically emits a spectrum of light proportional to the amount of energy absorbed.<sup>2</sup> This energy is in the form of ionization from secondary charged particles created by x-ray interactions. For diagnostic x-ray beams, the dominant interactions are incoherent scattering and photoelectric absorption.<sup>3</sup>

At the University of Florida (UF), a fiber-optic dosimetry system has been constructed and characterized to readily measure dose from diagnostic energy exposures.<sup>4,5</sup> The scintillating element consists of a plastic scintillator in the shape of a cylinder, 500  $\mu\text{m}$  in diameter, and a length of 3 mm. To transmit the scintillation photons from the sensitive element to the readout device, the scintillator is mechanically and optically coupled to an unjacketed multimode optical fiber with a diameter of 400  $\mu\text{m}$  and a length of 2mm. The other end of the optical fiber is connected with a photomultiplier tube (PMT).

The dosimetry system at UF is used in conjunction with the UF anthropomorphic phantoms, to obtain organ dose measurements.<sup>6</sup> These phantoms are constructed slice-by-slice using tissue-equivalent materials for soft tissue, bone, and lung. Slices

are stacked and bound together to form regions with corresponding anatomy and dose points to measure organ doses, which are delineated onto the top of each section. The FOC dosimeter's shape and flexibility allow for easy placement within the phantom and is capable of taking measurements in real time. The measured dose corresponds to the location of the scintillator within the phantom. Since the volume of the scintillator is so small, all measurements are typically referred to as point doses.

### **Organ Doses in Radiology Examinations**

Most diagnostic studies involving ionizing radiation consist of low energy x rays. The energy ranges between 10 and 120 keV depending on what type of imaging system is being utilized. With the exception of fluoroscopy, these procedures last on the order of seconds. As a result of the short time, most of the harmful effects are not physically observable and associated risk is mostly related to stochastic effects, carcinogenesis. Conventionally, cancer risk is evaluated using a metric called the effective dose. The effective dose is calculated by totaling the tissue-weighted organ doses of specific organs in the body that are most susceptible to stochastic effects from ionizing radiation. The formula for calculating effective dose from x rays is shown in Equation 1-1.

$$E = \sum_T w_T D_T * 1 \frac{Sv}{Gy} \quad (1-1)$$

The older method detailed by ICRP 26 for determining organ dose was to measure a point dose and use that value to model the dose of the organ.<sup>7</sup> ICRP 60 however specifies that all organ doses must be evaluated by averaging the dose across the

entire organ.<sup>8</sup> This quantity is much more accurate in quantifying organ dose, as the entire organ is evaluated compared to just a single point.

### **Objective**

The objective of this work focuses on the construction of an elongated FOC dosimeter that accurately measures the average organ dose from x-ray exposures pertaining to diagnostic studies in radiology. Current dosimeters used for in phantom measures, such as: thermoluminescent dosimeters (TLD's), ionization chambers, optical stimulated luminescence (OSL) detectors, and FOC detectors have such small sensitive volumes that they are modeled as point dosimeters. Most diagnostic studies expose only parts of the body necessary to image the anatomy critical for making a diagnosis. When part of the body is imaged, organs may be partially irradiated. This is especially relevant in CT where large organs such as the lung and liver are partially exposed. When taking dose measurements with point dosimeters, the dosimeter may be inside or outside the x-ray field and are therefore not representative of the average organ dose.

To account for the partial exposures and other dynamic organ dose profiles, a linear detector was investigated. This detector was fashioned as a fiber-optic coupled dosimeter with a scintillator length on the order of centimeters. An example of this is shown in Figure 1-1. The goal of this research is broken down into three sections, each of which is presented below.

1. The first aim is to investigate the feasibility of constructing a linear fiber-optic dosimeter. The work attempts to determine the theoretical response of the scintillator based on where the light was emitted and whether or not the effects due to the nature of fiber optics would significantly impair the response. This is also referred to as spatial sensitivity. The two specific effects investigated were attenuation within the scintillating fiber and the geometric coupling of the scintillating

and optical fiber surfaces. The scintillator response was modeled using MatLab simulations, based on fiber-optic principles.

2. The second aim was to develop and characterize the linear dosimeter to measure average absorbed doses within physical phantoms for diagnostic exposures under 120 kVp. Different sizes of sensitive elements were selected and characterized at diagnostic energies. The linear dosimeters offered excellent reproducibility, sensitivity to beam intensity and response to portion of sensitive element exposed.
3. The final objective was the application of this dosimeter as a collimation tool for mammography. The detector was evaluated for its accuracy in quantifying the x-ray to light field alignment. This is a mandatory quality control test done annually to maintain congruence between the x-ray and light fields. The accuracy of the detector was in measuring the x-ray-to-light field alignment was assessed.

### **Fiber-Optic Physics**

In scintillation detection, x-ray photons are detected through the energy transfer of x-ray photons into light photons by the process of scintillation. When a scintillating element absorbs energy, through collisions with electrons, light photons are emitted in proportion to the amount of energy absorbed. The physical principles of fiber optics allow for the capture and transmission of light to a readout device, most commonly a photo multiplier tube (PMT) that immediately digitizes the signal allowing for real-time measurement. When energy is absorbed in the scintillating fiber, light photons are emitted isotropically and are piped with little loss in intensity to the coupling side of the scintillator and transmitting fiber. Light is transmitted into the transmission fiber through refraction and internally reflected through the fiber to the PMT. The numerical aperture characterizes the relative amount of light transmitted into the transmission fiber from light produced in the scintillating fiber. This quantity is dependent on the optical properties of both fibers. Light is also lost at the coupling interfaces as well as transmission losses inside the fiber. Beddar models the collection efficiency of a fiber optic system as shown in Equation 1-2.<sup>9</sup>

$$\epsilon = \epsilon_{\text{accept}} \epsilon_{\text{couple 1}} \epsilon_{\text{couple 2}} \epsilon_{\text{transmit}} \quad (1-2)$$

The last term in Equation 1-2 represents the transmission efficiency of the scintillating and transmission fiber accounting for attenuation of light photons inside the fibers due to transmission. The two coupling terms describe the losses in light from the coupling of the scintillating fiber to the transmission fiber, and the transmission fiber to the PMT. Most of the losses in signal can be attributed to light falling outside the acceptance cone of the transmission fiber. The acceptance efficiency for the optical fiber, assuming isotropic emission, can be modeled as the ratio of the acceptance cone of the optical fiber over total solid angle of emission. The acceptance cone of the optical fiber is a function of the maximum acceptance angle. The number of incident light photons that fall within a cone parameterized by the maximum acceptance angle will reach the PMT. The maximum acceptance angle,  $\theta_{\text{max}}$  is defined by Equation 1-3.

$$\theta_{\text{max}} = \sin^{-1} \left\{ \frac{\sqrt{n_1^2 - n_2^2}}{n_0} \right\} = \sin^{-1} \left( \frac{NA}{n_0} \right) \quad (1-3)$$

Where  $n_1$  and  $n_2$  are the index or refraction of the core and cladding respectively of the transmitting fiber,  $n_0$  is the index of refraction of the scintillating fiber core, and NA denotes the numerical aperture of the optical fiber and characterizes the angle of internal reflection within the fiber. The acceptance efficiency is quantified in Equation 1-4 as the ratio of the volume of the acceptance cone to the total solid angle.

$$\epsilon_{\text{accept}} = 2 * \frac{1}{4\pi} \int \sin\theta d\theta d\beta \quad (1-4)$$

The efficiency is doubled to represent the assumption that all light emitted in the opposite direction to the optical fiber will be reflected back into the fiber by a reflector.

Additionally, Beddar claims that with most FOC dosimeters, losses in coupling and transmission are an order of magnitude greater.

The acceptance efficiency of the fiber system could be potentially affected if the acceptance cone, described by Equation 1-4, is greater than the transmission cone of the scintillating fiber. Further down the fiber axis from the coupling surface, fewer scintillation photons will reach the end of the transmission fiber un-reflected. To reach the transmission fiber the reflected photons will have to fall within the transmission cone of the scintillating fiber. Issues could arise if this cone were less than the acceptance cone of the optical fiber, as photons emitted closer to the coupling end would be more likely to be detected than the majority of photons emitted further down the fiber axis would have to undergo reflection to reach the transmission fiber. The transmittance cone of the scintillator,  $\alpha$ , as described in Equation 1-5, is derived from the critical angle for internal reflection within the fiber centered on to the horizontal axis normal to the cross section of the fiber. The angle for internal reflection is characterized by Snell's Law for indices of refraction  $n_{\text{clad}}$  and  $n_{\text{core}}$ , also  $n_0$  in Equation 1-3, of the scintillating fiber.

$$\alpha = \frac{\pi}{2} - \sin^{-1} \left( \frac{n_{\text{clad}}}{n_{\text{core}}} \right) \quad (1-5)$$

Figure 1-2 illustrates the acceptance and transmittance cone of the transmission and scintillating fiber, represented by  $\theta$  and  $\alpha$  respectively. Using the index of refraction for the cladding (1.49) and the core (1.60), the solid angle  $\alpha$  for transmitting light through the scintillator was calculated to be  $42.74^\circ$ .<sup>10</sup> The transmission fiber has a numerical aperture of 0.22, resulting in an acceptance cone  $\theta$  calculated using Equation 1-3 of  $15.81^\circ$ .<sup>11</sup> Therefore light emitted close to the coupling edge holds no preference over

light emitted distally. Because the collection efficiency with respect to the origin of the scintillated light photon within the scintillating fiber remains unchanged with regards to distance along the fiber's axis, the acceptance efficiency should be unaffected by the location light producing events within the scintillation fiber.

### **Linear Detector Feasibility**

This section is dedicated to theoretically predicting the feasibility of a linear FOC detector as an accurate tool for evaluating absorbed dose. The first section will examine attenuation of light inside the optical fiber and how that will impact the spatial sensitivity of the detector. The attenuation of light inside a scintillating fiber is caused by imperfections at the core-cladding interface, reabsorption of light, and Rayleigh scattering of light deflecting photons outside the transmission cone. The effect of coupling of the two fibers was also evaluated. The coupling effect is induced by the different diameters of the transmission and scintillating fibers. The geometry of the fibers and the different surface areas may have a significant effect on the fibers' spatial sensitivity as well. Therefore, this was also investigated.

### **Attenuation Effects on Spatial Sensitivity**

Factors potentially affecting the spatial sensitivity are attenuation within the scintillating fiber and signal degradation due to uncoupled surfaces on the scintillating fiber that lead to escaped light photons. Assuming light is emitted isotropically, light from one end of the fiber will travel a different path length than light emitted from the opposite end. Additionally, light that travels at an angle closer to the acceptance angle will undergo more reflections than light propagating parallel to the axis orthogonal to the coupling surface. This would also result in a longer path length. The fraction of light

attenuated by the scintillating fiber  $F(x)$  with respect to distance along the fiber axis,  $x$ , is described by Equation 1-6.

$$F(x) = \frac{1}{2} \frac{\left[ \int_0^{\theta_c} e^{-\frac{1}{\lambda} x \sec \theta} e^{-\frac{1}{\lambda'} L' \sec \theta} d\theta \right]}{\int d\theta} + \frac{1}{2} \epsilon \frac{\left[ \int_0^{\theta_c} e^{-\frac{1}{\lambda} (2L-x) \sec \theta} e^{-\frac{1}{\lambda'} L' \sec \theta} d\theta \right]}{\int d\theta} \quad (1-6)$$

The terms  $L$  and  $L'$  specify the length of the scintillator and the fiber respectively, and the terms  $\lambda$  and  $\lambda'$  describe the linear photon attenuation coefficients of those fibers. The integral is independent of radial distance from the central fiber axis because although it will induce one additional reflection it does not change the total distance traveled within the scintillator. The number of reflections for a given distance from the coupling surface at an angle less than the critical angle remains relatively constant because the transmittance angle in the scintillating fiber is greater than the acceptance angle of the optical fiber. All angles less than the acceptance angle of the optical fiber will be internally reflected inside the scintillating fiber. The exponential is integrated over the acceptance angle of the optical fiber.  $\theta_c$  represents the largest angle of light emitted that could fall within the acceptance cone of the optical fiber. The integration was performed numerically at 1.0 mm intervals in MATLAB<sup>®</sup> (Mathworks, Natick, MA). The results are displayed in Table 1-1 for a reflector efficiency of 95%, scintillating fiber attenuation coefficient of  $0.00037 \text{ mm}^{-1}$ , optical fiber attenuating coefficient of  $0.00012 \text{ mm}^{-1}$  optical fiber of length 2 m and scintillating fiber of length 16 cm.

Equation 1-6 models light attenuation for meridional rays. These types of rays pass through the axis of the optical fiber and propagate in a single plane. Meridional rays only make up a fraction of the light transmitted through the fiber. The other type of transmitting waves are skew rays, which propagate in a helical path without passing

through the center axis of the fiber and usually outnumber meridional rays because of a larger acceptance cone. Figure 1-3 illustrates the ray propagation defined in two planes. The acceptance angle is shown to be:

$$\theta_a = \sin^{-1} \left( \frac{\sqrt{(n_{core}^2 - n_{clad}^2)}}{n_{scint} \cos \gamma} \right) \quad (1-7)$$

The cosine term represents the angle of reflection for skew rays ( $\gamma$ ) within the fiber. Using the critical angle of internal reflection within the optical fiber ( $70.51^\circ$ ), the acceptance angle was determined to be  $24.3^\circ$ . Kühlen, defined an approximate equation for the attenuation path length  $\lambda$  as a function of emittance angle for both meridional and skew waves inside a fiber, length  $d$  from the detector.<sup>12</sup>

$$\frac{1}{\lambda} = \frac{1}{\lambda_b \cos \theta} + \frac{\ln\left(\frac{1}{R}\right) 4 \tan \theta}{\pi D} \quad (1-8)$$

Where  $D$  is the diameter of the fiber,  $R$  is the reflection coefficient,  $\lambda_b$  is the attenuation coefficient defined as  $\lambda$  in Equation 1-6, and  $\theta$  is the emitted angle. The first term in the equation represents attenuation of meridional rays and the second term represents the attenuation component from skew rays. Using this model, another MATLAB simulation was run using the same parameters. The reflectivity coefficient  $R$  was estimated to be 0.9997 and the diameter of the fiber is 0.5 mm. The results of these simulations are tabulated in Table 1-2, and plotted in Appendix B. The acceptance angle for the plastic optical fiber for skew rays is  $69.5^\circ$ .

Attenuation of light photons due to transmission thru the scintillating fiber proved to be a small and negligible effect. Applying a linear fit to the results from Table 1-2, the

attenuation per length of scintillator can be expressed as 0.0131%/cm. The attenuation of signal was slightly more when including both types of rays.

### **Coupling Effects on Spatial Sensitivity**

The coupling surface geometry of the fibers also potentially plays a role in the spatial sensitivity of the scintillating fiber. Uncoupled areas on the scintillator will result in a loss of transmitted signal to the optical fiber through refraction of the light photon into the surrounding medium, which in most cases is air. A MATLAB program was developed to simulate meridional light detection for a uniform exposure. Light was assumed to be emitted isotropically, and was considered a detected photon if it was incident on the optical fiber at an angle within the acceptance cone described by Equation 1-3. The optical fiber, smaller in diameter, was modeled as being centered on the scintillating fiber leaving a uniform uncoupled cross-section. Other assumptions included the disregard of reflection at the uncoupled surface at all incident angles, and light escaping the scintillating fiber and re-entering through the optical fiber. The results for a 4-cm fiber are plotted in Figure 1-4.

The geometric coupling efficiency for an optical fiber with diameter  $D_2$  aligned axially and coupled to a scintillating fiber with diameter  $D_1$  could be estimated as the ratio of the diameters of the optical fiber to scintillating fiber for light internally reflected in a single plane. For skew rays the efficiency could be estimated as a ratio of the areas of each fiber as the ray propagates throughout the cross-section of the fiber. The results show a negligible difference in amount of detected photons with respect to distance along the fiber axis, especially after 0.5 cm, the distance beyond which a significant portion of the meridional waves must undergo multiple reflections.

Table 1-1. Fiber attenuation of meridional rays at locations distal from the coupling surface. Data produced from MATLAB code in Appendix A.

Distance (cm)	% attenuation
0	27.17%
2	27.21%
4	27.24%
6	27.27%
8	27.30%
10	27.33%
12	27.35%
14	27.37%
16	27.38%

Table 1-2. Fiber attenuation of both skew and meridional rays at locations distal from the coupling surface. Data produced from MATLAB code in Appendix B.

Distance (cm)	% attenuation
0	27.48%
2	27.52%
4	27.56%
6	27.60%
8	27.63%
10	27.66%
12	27.68%
14	27.70%
16	27.72%

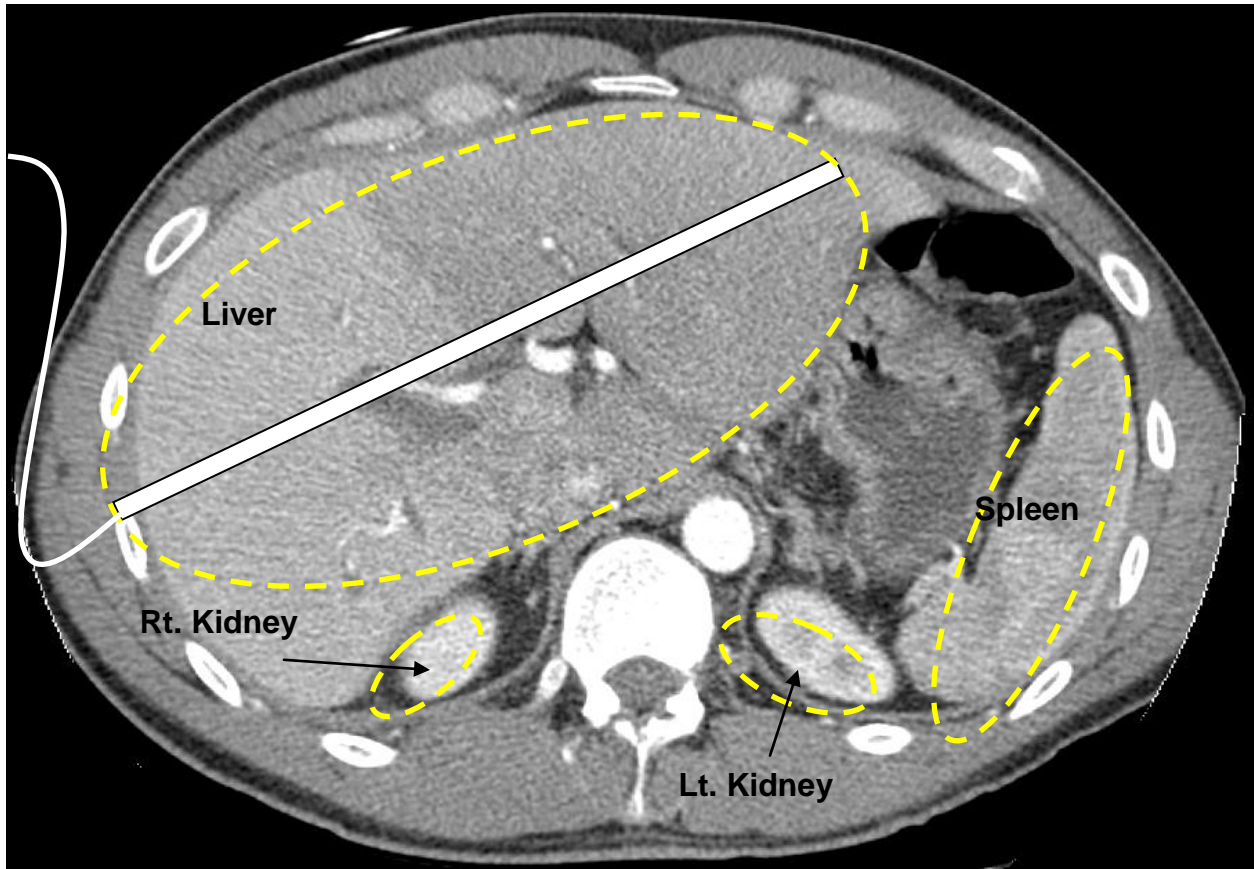


Figure 1-1. Schematic illustrating the position of a linear dosimeter in relation to the organ of interest.

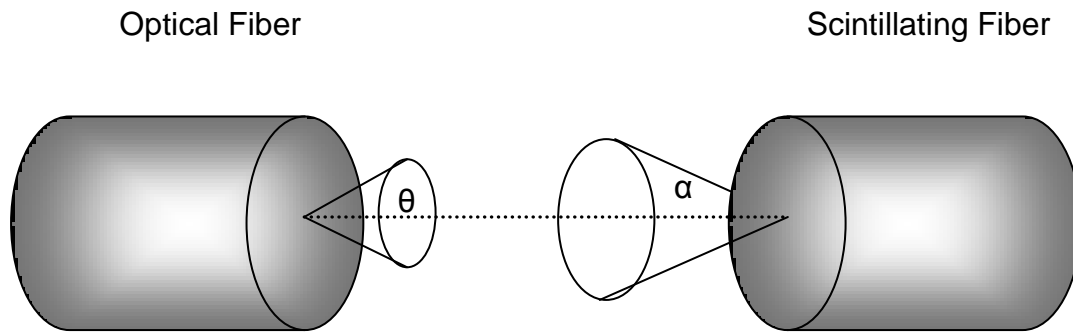


Figure 1-2. Diagram illustrating the acceptance and transmission cone of the scintillating and optical fiber, characterized by angles  $\alpha$  and  $\theta$ .

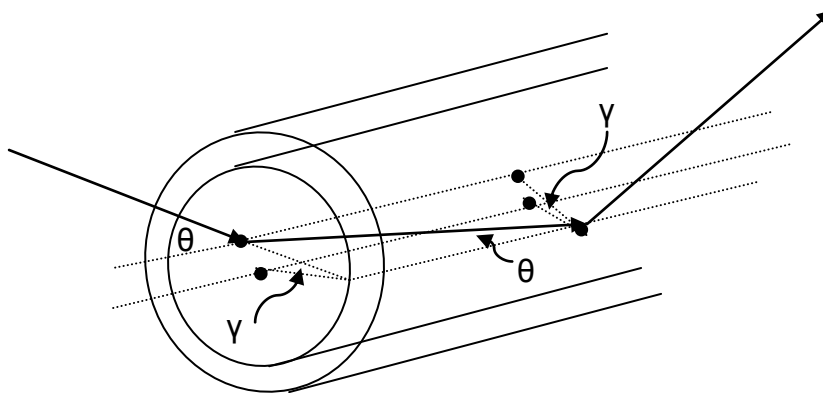


Figure 1-3. Illustration of a skew ray internally reflected inside an optical fiber. The reflection is described by angles  $\theta$  and  $\gamma$ .

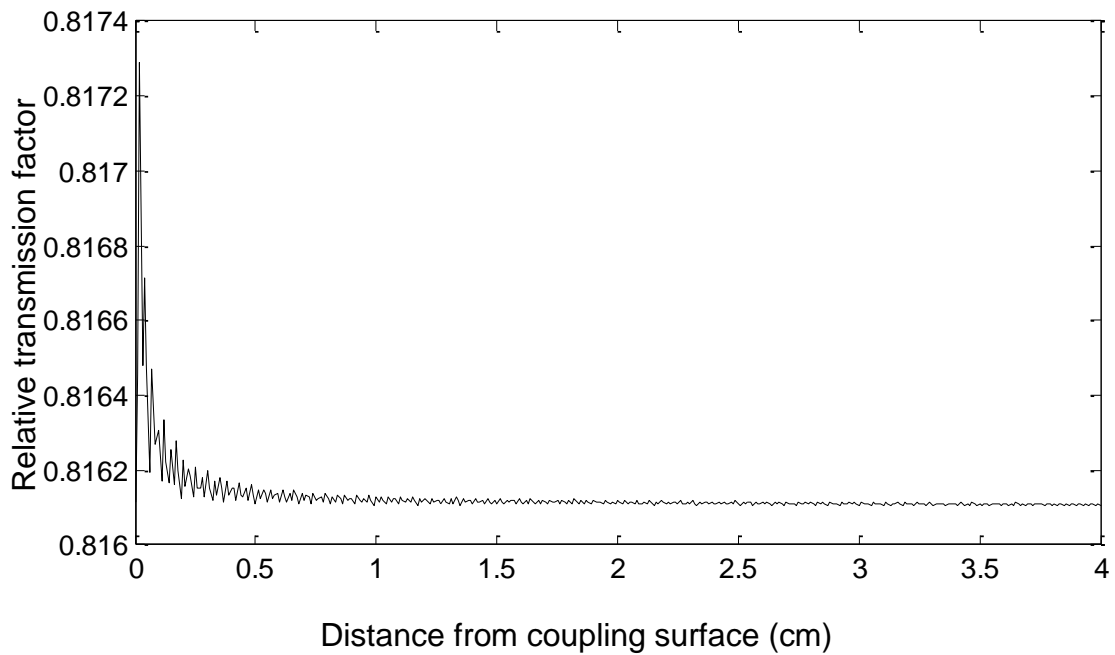


Figure 1-4. Relative transmission of light through the coupling surface at locations along the scintillating fiber's axis. The simulation is run for a scintillating fiber, diameter of 0.5 mm, and a transmitting fiber, of diameter 0.4 mm. Coupling was modeled so that both of the fiber's axes were aligned with one another.

## CHAPTER 2 CHARACTERIZATION OF A LINEAR FIBER-OPTIC COUPLED DOSIMETER

### **Introduction**

The novel concept of using an elongated scintillating fiber to detect x-ray photons can certainly be applicable to radiation dosimetry. The materials used in the FOC system are water equivalent, and have been characterized and utilized to measure absorbed dose for diagnostic energy x-ray beams, described in the paper by Hyer.<sup>13,14</sup> FOC dosimeters are proven to be useful for in-phantom dosimetry due to their small size and overall flexibility. Comparable diagnostic energy range detectors such as ionization chambers, thermoluminescent dosimeters (TLDs), or optically stimulated luminescent (OSL) dosimeters are either too large to incorporate into phantoms or require time consuming reading processes after irradiation to extract dose information. FOC dosimeters also overcome the shortfalls of other instruments by displaying minimal angular dependence, no detectable degradation over time, high reproducibility, and real-time output monitoring.

The capability of taking linear dose measurements compared to point dose measurements allows for more accuracy in quantifying the organ dose leading to an improved methodology for determining the effective dose. When applying this new system to CT dosimetry, the energy dependence, documented in Hyer's investigation of FOC dosimeters, may also be minimized since the sensitive element of the fiber is located along different depths within the phantom, and may be averaged out due to the helical motion of the x-ray tube. The work in this section characterizes the elongated scintillating fiber FOC system for diagnostic energies low enough that the production of Cherenkov radiation in the optical fiber is not a concern.<sup>15</sup> The characterization

parallels the methods used by Hyer with an end result of a dosimeter capable of accurately measuring real-time in-phantom doses within the diagnostic energy range.

### **Materials and Methods**

The dosimeter was developed by modifying the fiber-optic coupled (FOC) dosimetry system at the University of Florida. Fiber construction was accomplished using the same techniques used by both Tien and Hyer. The plastic scintillating fiber (BCF-12, Saint-Gobain Crystals, Nemours, France), which was previously 3 mm in length, was replaced to mirror the dimensions of organs for the University of Florida adult anthropomorphic phantom. Therefore, a series of six fibers were fashioned to scintillating fiber lengths of: 3.0, 5.0, 7.0, 10.0, 12.0, and 15.0 centimeters. The diameter of the fiber is small enough to avoid the effects of varying intensity across the x-ray field caused by the heel effect or any other type of nonuniform x-ray field conditions. One end of the scintillating fiber was coupled to a multi-mode transmission optical fiber (400-UV, Polymicro Technologies., Phoenix, AZ), having a 400- $\mu\text{m}$  diameter, and two meters in length. Before coupling, both ends were polished to improve coupling efficiency. The transmission fiber functions as a light pipe, transmitting light produced in the scintillating fiber to the readout device. The remaining end of the scintillator was coated with reflective paint (EJ-510, Eljen Technology, Sweetwater, TX) to increase the acceptance efficiency of the fiber optic system. The coupled scintillating-transmission fiber assembly is encased in heat-shrink tubing, mounted to a SMA connector (SMA-490, Ocean Optics Inc., Dunedin, FL) and sealed to prevent light entering and escaping. The area of heat-shrink tubing covering the scintillating fiber was spray painted to allow the user to optically align the detector to the organ of interest for phantom measurements. A serial port interface on the PMT

(Hamamatsu Corporation, Bridgewater, NJ) permits real-time monitoring of the detector output via a custom computer program. The PMT was chosen specifically to match its quantum detection efficiency with the emission peak of the scintillator (430 nm).<sup>16</sup> An array of PMT detectors allows multiple detector assemblies to be evaluated simultaneously.

The characterization of the FOC dosimeter was performed using a clinical x-ray tube with filtration of 5.60 mm Al at 120 kVp and a fixed field size of 4.5 x 4.5 cm. All measurements were taken 112 cm from the target using a custom built tissue-equivalent phantom. One phantom was built to house the dosimeter and the other to accommodate a 10-cm pencil chamber. Within both phantoms the detectors were positioned so that 1.2 cm of tissue equivalent material covered the top and bottom of each detector. The tissue equivalent material is the same material composition used for the University of Florida anthropomorphic phantoms and will be further known as soft tissue equivalent substitute (STE). Several x-ray tube potentials of 60, 70, 80, 90, 100, 110, and 120 kVp corresponding to measured half value layers of 2.9, 3.47, 3.86, 4.23, 4.83, 5.24, and 5.6 mm Al and x-ray tube current-time products ranging from 32 to 400 mAs, were used to expose the dosimeters. All measurements were repeated five times to reduce statistical uncertainties and provide reliable reproducibility measurements. A 10-cm pencil chamber and associated electrometer (chamber model RC3CT, electrometer model, RadCal Corporation, Monrovia, CA) were used to provide simultaneous exposure measurements.

## **Results**

The energy dependence of the FOC dosimeter was evaluated using the tissue equivalent phantom with the ionization chamber and fiber at a depth of 1.2 cm in the

STE. The x-ray tube potentials ranged from 60 to 120 kVp with 10 kVp increments. The 10-cm pencil ionization chamber was irradiated separately and at the same position, to account for a non-uniform field, but under the same field size and source-to-detector distance. The 10-cm FOC dosimeter was used to match the geometry of the pencil ion chamber. The normalized detector readings, in counts/mGy, were plotted against tube potential, seen in Figure 2-1, and entrance half-value layer, Figure 2-2. The results were normalized to the 120 kVp and 5.6 mm Al data point. The response is shown to be positively linear, with an average 4.4% increase per 10 kVp, and 9.8% per mm Al across the depicted energy and half-value layer range.

The effect of varying beam quality due to x-ray attenuation at different depths within soft tissue was also evaluated. The same 10-cm dosimeter and pencil ion chamber were placed in their respective phantoms and measurements were taken at different depths within the STE and expressed in terms of counts/mGy. The results were normalized to the 1.2 cm measurement and used to create a series of plots of the normalized dosimeter sensitivity versus depth in the STE for x-ray beams with peak tube potentials of 120, 100, 80, and 60 kVp. These plots are depicted in Figure 2-3, 2-4, 2-5, and 2-6 respectively. The raw data for each of the dosimeters was also used to render the percent depth dose (PDD) curves for the four x-ray beams. The sensitivity of the dosimeter increases at greater depths within the STE. This effect can be attributed to the detectors energy dependence, in addition, the effects of beam hardening at greater depths. This effect shows a variation of 8% across the range of depths investigated. The PDD curves for the four evaluated x-ray beams are shown in Figure 2-7.

Figure 2-8 plots the response of the 7-cm and 15-cm scintillating fiber response to beam intensity. The linearity of the scintillating element, with respect to x-ray tube current, was evaluated by increasing the time-current product from 32 to 400 mAs while maintaining the tube potential at 120 kVp. The pencil ionization chamber was used as a means to quantify the tissue kerma for each exposure. Both the fiber and ionization chamber measurements were taken using the STE phantoms. A linear fit was applied to the data to provide a correlation coefficient which characterized the linearity of the fibers. This coefficient was found to be 0.9999, demonstrating the fibers exhibit excellent linearity with respect to beam intensity. A linear trend line was also applied to the plot. The slope of the linear function is expressed in terms of thousand counts/mGy. Error bars were removed because they were too small to be displayed.

The spatial sensitivity was evaluated for the series of dosimeters by evaluating the response to the length of scintillating fiber irradiated in the x-ray field at diagnostic energies. Six scintillators, with sensitive element lengths of 3.0, 5.0, 7.0, 10.0, 12.0, and 15.0 centimeters were tested. The dosimeters were placed in a custom STE phantom at a depth of 1.2 cm of material above and below the dosimeter. A step motor was used to insert each dosimeter incrementally into the x-ray field generated by a clinical portable x-ray unit at 80 kVp and 10.5 mAs. Sensitivity was measured in number of measured counts as a function of exposed scintillating fiber length (sensitive region) at 0.5 cm intervals. The results are displayed in Figures 2-9 through 2-14. A linear fit was applied in order to obtain the number of counts per centimeter of exposed fiber and along with the linear correlation coefficient. The linearity of the dosimeters proved to be excellent with an average linear correlation coefficient of 0.996.

Table 2-1 and Table 2-2 summarize the mean counts measured and standard deviation over the exposed range of interest commonly found in diagnostic radiology for both the -cm and 15-cm detectors. The coefficient of variation (COV) was found to be an order of magnitude less for the 15-cm dosimeter. At lower tissue kerma levels, the COV was larger, which is attributed to a lower number of overall measured counts. The COV for either fiber was found to be 1.25% at 1.87 mGy.

### **Discussion**

The dosimeters demonstrate an exceptional linear response with beam intensity and a positive linear energy dependence within the exposure range of radiographic and CT imaging devices. An excellent spatial sensitivity was observed for each of the six fibers. The lowest linear correlation coefficient was found to be 0.9933. A depth dependence was also observed as a result of energy components introduced from beam hardening and the addition of a scatter component. The overall energy dependence indicates an increasing linear trend with respect to x-ray tube potential. To correct for this effect the dosimeter would be required to be calibrated at every evaluated depth and beam energy. The variation in sensitivity of the fiber was approximately 4.4% per 10keV and 8% across 11 cm of the STE. One of the benefits of CT is that the dynamic motion of the gantry tends to reduce the effects of beam hardening leading to a decreased variation in sensitivity.

A higher coupling efficiency proves to lower the COV and improve the linear correlation coefficient. Although the coupling efficiency of each dosimeter could not be quantified, the slope of the spatial sensitivity plots provided a relative metric. The slopes from each dosimeter and the average standard deviation are listed in Table 2-3. The range in counts/cm for the evaluated dosimeters ranged from 3,000 to 10,000.

The angular dependence of the detector was not evaluated. However, this information has previously been characterized for the point FOC dosimeter, and can be found in Hyer's paper. Due to the geometry of the elongated scintillating fiber, the normal-to-axial angular dependence should improve, while the axial dependence will remain unchanged. The angular dependence is most affected when the un-collided x-ray fluence enters the sensitive region from the coupling side resulting in a lower number of detected counts. The improvement is due to the increased surface area around the axis of the sensitive element. For a 3-mm scintillating fiber this ratio is 12, compared to 200 for a 5-cm fiber. However, In CT dosimetry, the effect of these variations will likely be averaged out for in-phantom measurements due to the rotation of the x-ray tube and scatter.

### **Conclusion**

The linear FOC dosimeter in this study mirrors the response of the point FOC dosimeter evaluated by Hyer. Both shared an exceptional linear response to beam intensity and a positive energy and depth dependence. The reproducibility of each fiber can be characterized with a COV ranging from 0.5% to 2%, with the extended scintillating FOC detector geometry showing a slightly lower variation in detected counts, due to the higher light output from the scintillating fiber. The energy dependence is minimized by calibrating the detector at several depths of material to account for varying beam quality with depth dependence due to beam hardening and scattering. Overall, this type of detector appears most appropriate for measuring organ doses, where the scintillating element can be fashioned to the dimensions of the organ being evaluated. The rotating x-ray tube will minimize the angular dependence of the fiber as well as flatten the depth dose profile. In addition to providing rapid and accurate

measurements, when properly calibrated, this type of FOC dosimeter demonstrates exceptional utility for in-phantom CT organ dose measurements.

Table 2-1. Reproducibility of measurements with 7-cm FOC dosimeter

Tissue kerma (mGy)	Mean counts	Standard deviation	COV (%)
1.50	15289	165.12	1.080
1.87	18916	236.45	1.250
2.93	29578	300.22	1.015
3.73	37333	176.96	0.474
4.68	46830	220.57	0.471
5.85	58691	117.38	0.200
7.50	75156	95.44	0.127
18.77	189022	489.89	0.256

Table 2-2. Reproducibility measurements with 15-cm FOC dosimeter

Tissue kerma (mGy)	Mean counts	Standard deviation	COV (%)
1.50	110062	236.17	0.215
1.87	135945	487.68	0.359
2.93	210977	490.81	0.233
3.73	264227	1090.82	0.413
4.68	323149	425.21	0.132
5.85	395438	212.08	0.054
7.50	506237	256.19	0.051
18.77	1272686	1958.27	0.154

Table 2-3. Dosimeter sensitivity

Linear FOC (mm)	Slope ( $10^3/cm$ )	Standard deviation
30	10.054	80.7
50	3.2354	76.1
70	2.9178	83.2
100	3.1102	119.7
120	6.8743	162.1
150	10.31	205

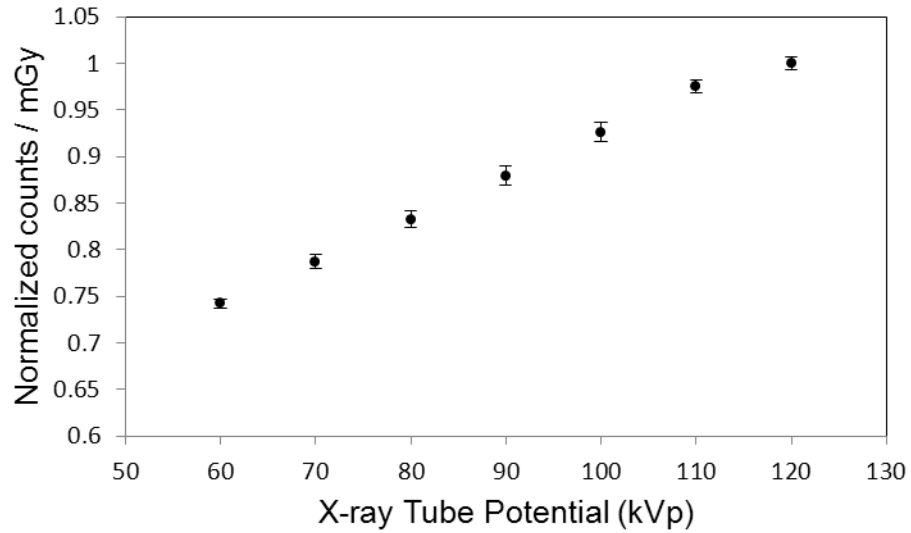


Figure 2-1. Energy dependence of the dosimeter to peak tube potentials within the range used in radiology. Error bars correspond to  $\pm 1$  standard deviation of the mean. Data was normalized to the 120 kVp data point. The linear correlation coefficient was determined to be 0.966

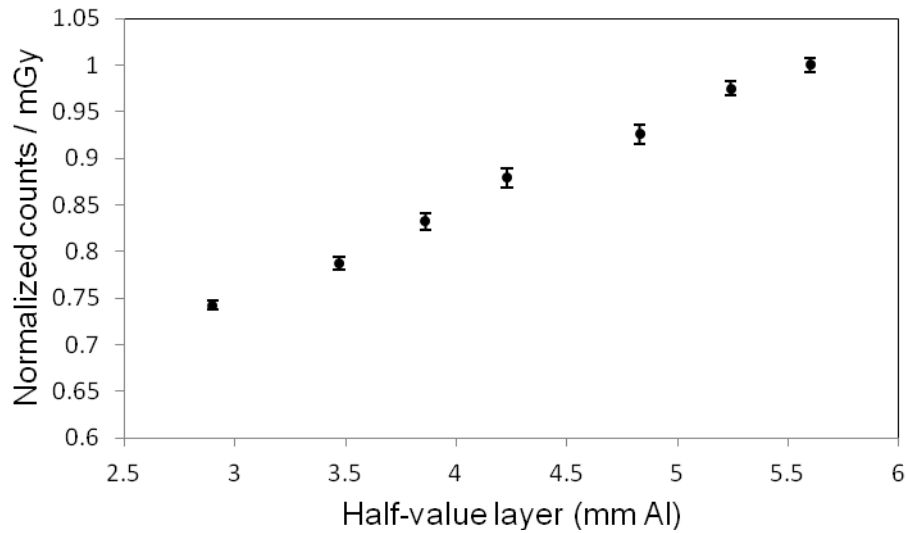


Figure 2-2. Energy dependence of the dosimeter to half-value layers within the range used in radiology at various tube potentials. Error bars correspond to  $\pm 1$  standard deviation of the mean. Data was normalized to the 5.6 mm Al data point. The linear correlation coefficient was determined to be 0.966.

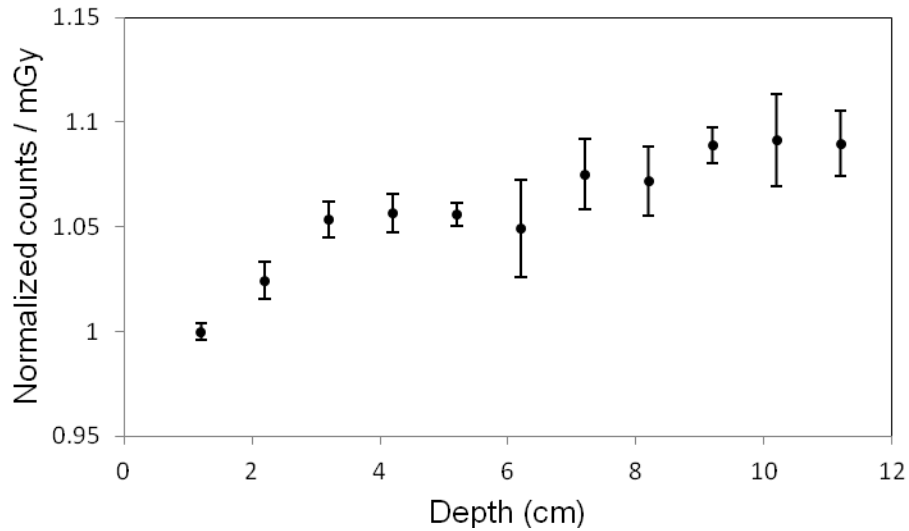


Figure 2-3. Energy dependence of the dosimeter as a function of depth in soft tissue-equivalent material (STE) material for an incident x-ray beam characterized by a half-value layer of 5.6 mm Al and 120 kVp. Data has been normalized to the 1.2 cm-measurement. Error bars correspond to  $\pm 1$  standard deviation of the mean.

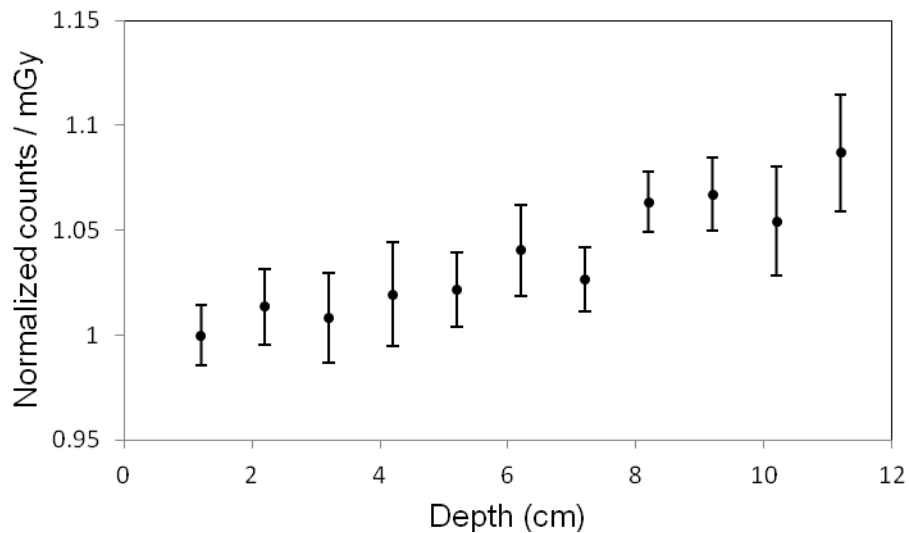


Figure 2-4. Energy dependence of the dosimeter as a function of depth in soft tissue-equivalent material (STE) material for an incident x-ray beam characterized by a half-value layer of 4.83 mm Al and 100 kVp. Data has been normalized to the 1.2 cm-measurement. Error bars correspond to  $\pm 1$  standard deviation of the mean.

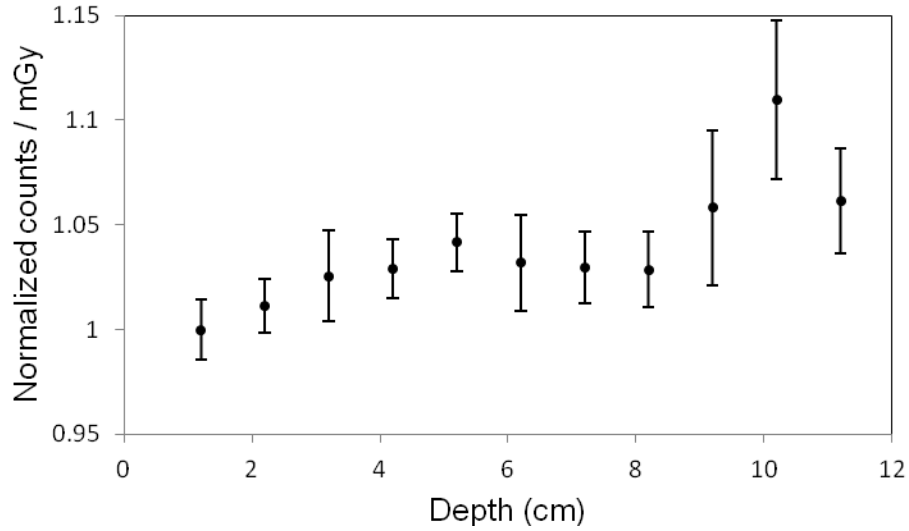


Figure 2-5. Energy dependence of the dosimeter as a function of depth in soft tissue-equivalent material (STE) material for an incident x-ray beam characterized by a half-value layer of 3.86 mm Al and 80 kVp. Data has been normalized to the 1.2 cm-measurement. Error bars correspond to  $\pm 1$  standard deviation of the mean.

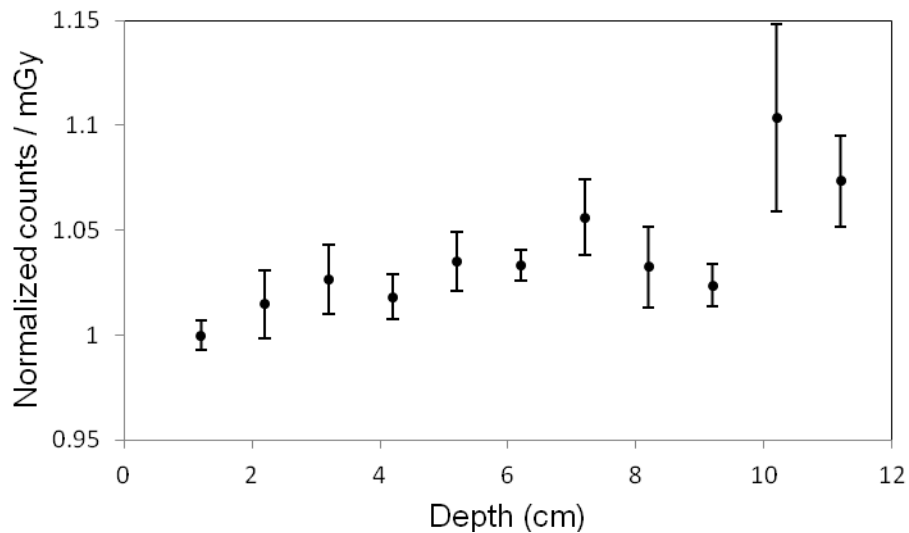
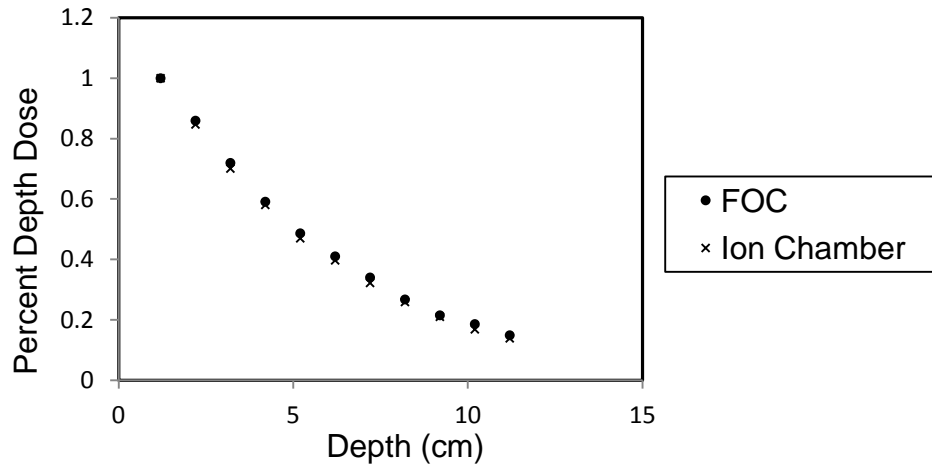


Figure 2-6. Energy dependence of the dosimeter as a function of depth in soft tissue-equivalent material (STE) material for an incident x-ray beam characterized by a half-value layer of 2.9 mm Al and 60 kVp. Data has been normalized to the 1.2-cm measurement. Error bars correspond to  $\pm 1$  standard deviation of the mean.

A)



B)

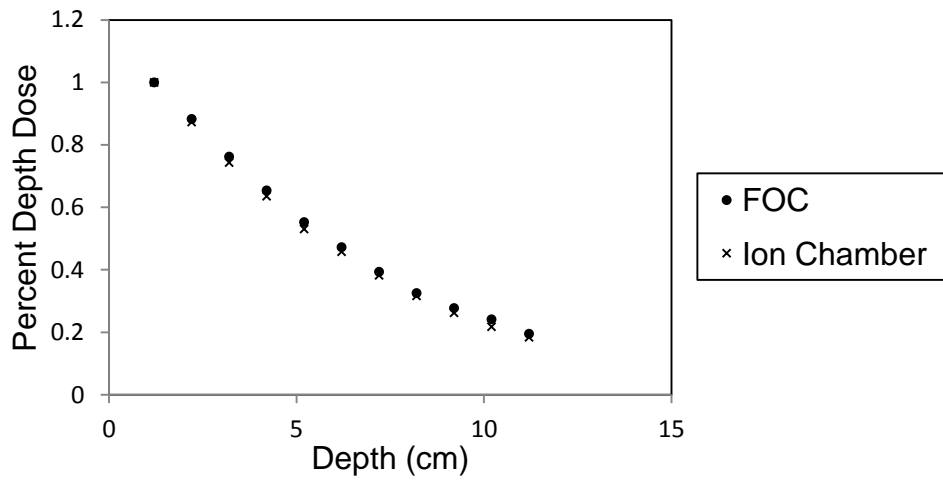
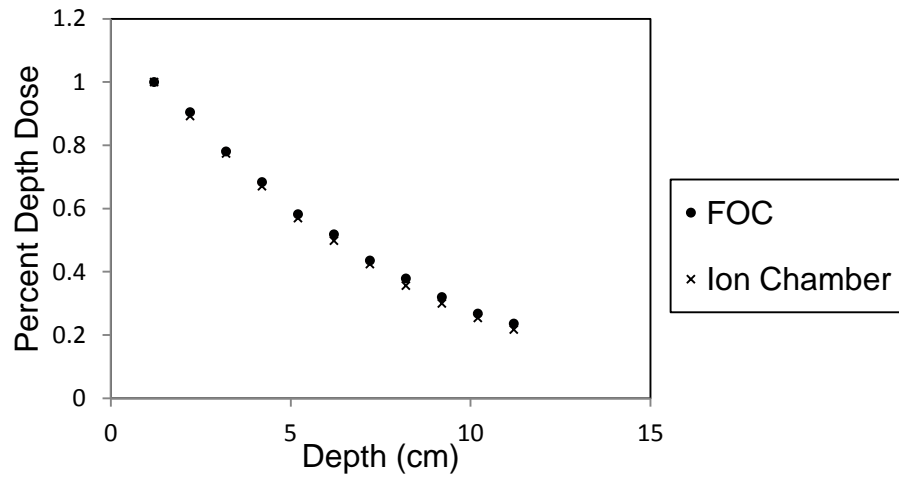


Figure 2-7. Percent Depth Dose curves of the ion chamber and FOC dosimeter for various beam qualities. A) 2.9 mm Al B) 3.86 mm Al C) 4.83 mm Al D) 5.60 mm Al. Error bars are not displayed because of visual obstruction of data. PDD curves are normalized to the 1.2 cm data point for both detectors.

C)



D)

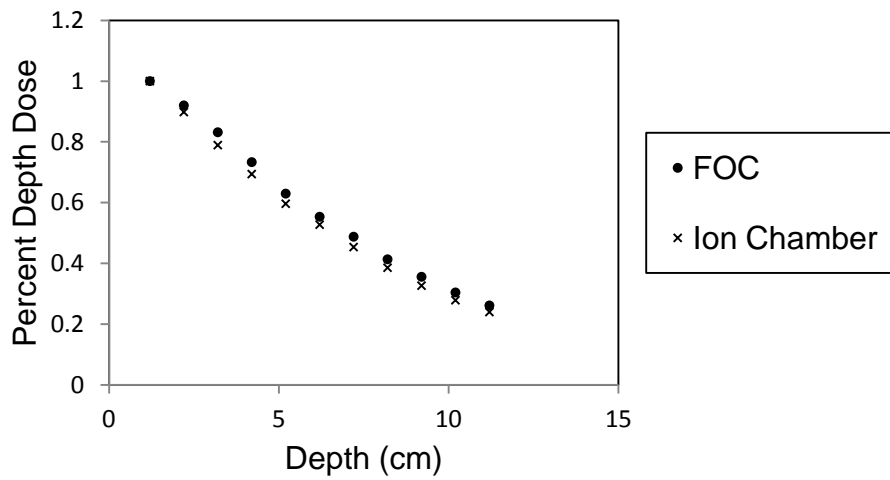
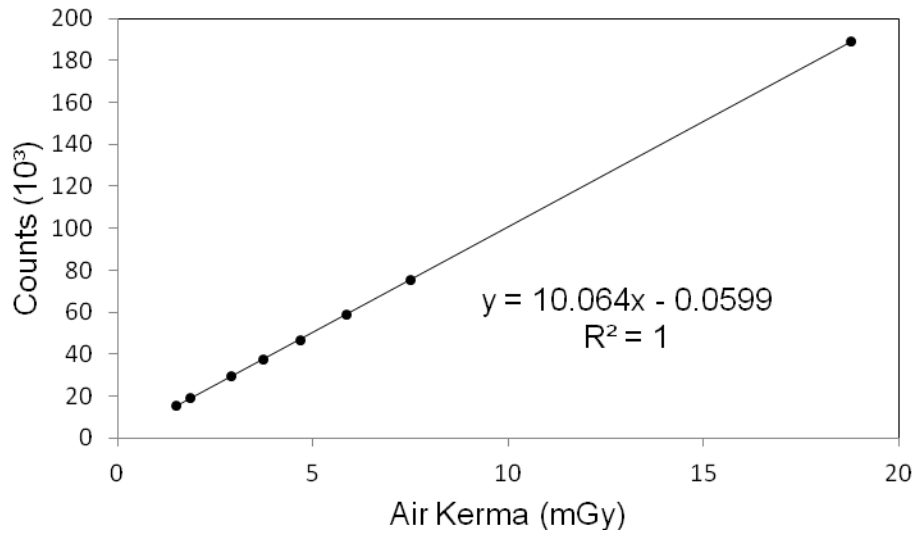


Figure 2-7. Continued.

A)



B)

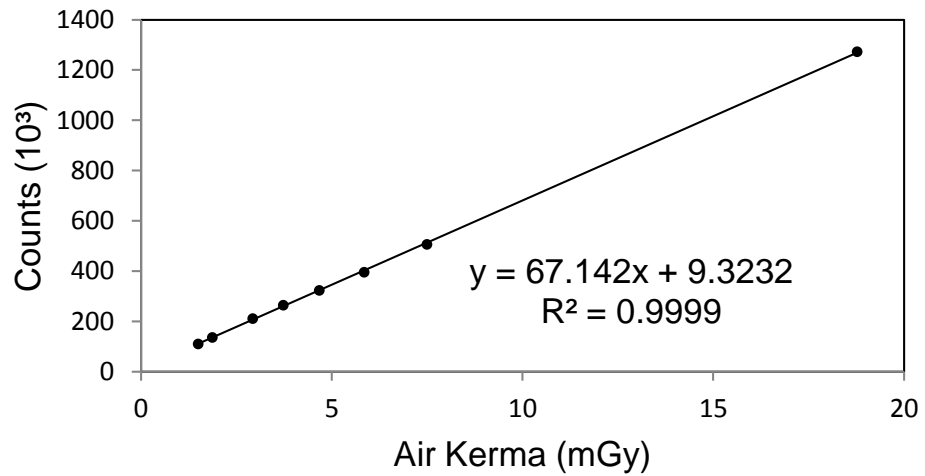


Figure 2-8. Linearity of FOC dosimeter to beam intensity. A) 7cm sensitive element B) 15 cm sensitive element. The dose in mGy is the dose in air within the tissue equivalent material (STE).

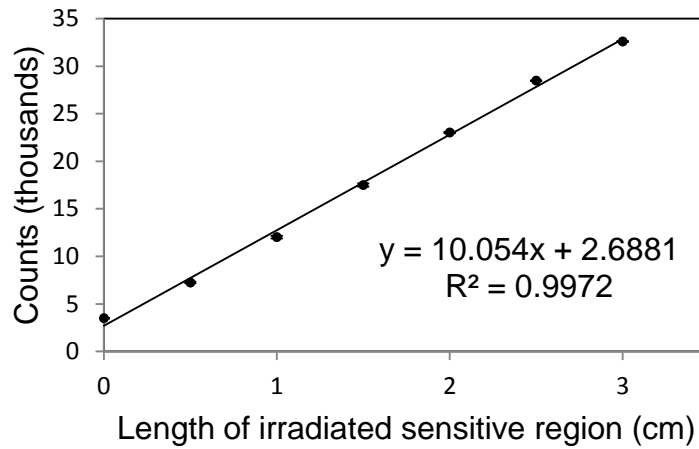


Figure 2-9. Spatial sensitivity of the 3cm FOC dosimeter. Linear fit was applied to the data along with a linear correlation coefficient. Error bars correspond to  $\pm 1$  standard deviation of the mean.

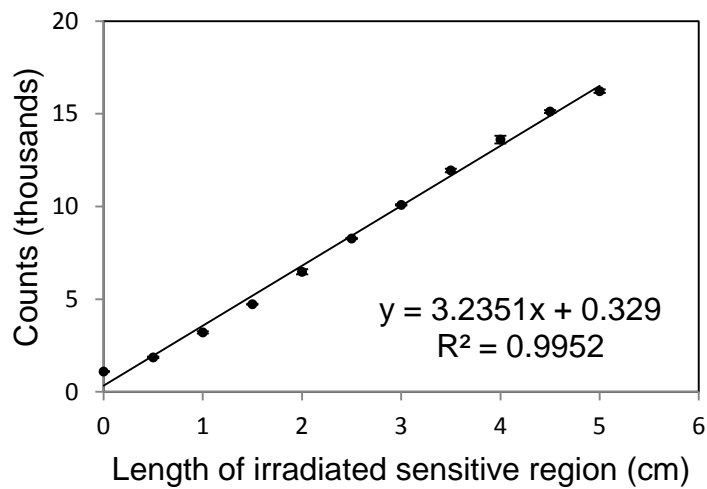


Figure 2-10. Spatial sensitivity of the 5cm FOC dosimeter. Linear fit was applied to the data along with a linear correlation coefficient. Error bars correspond to  $\pm 1$  standard deviation of the mean.

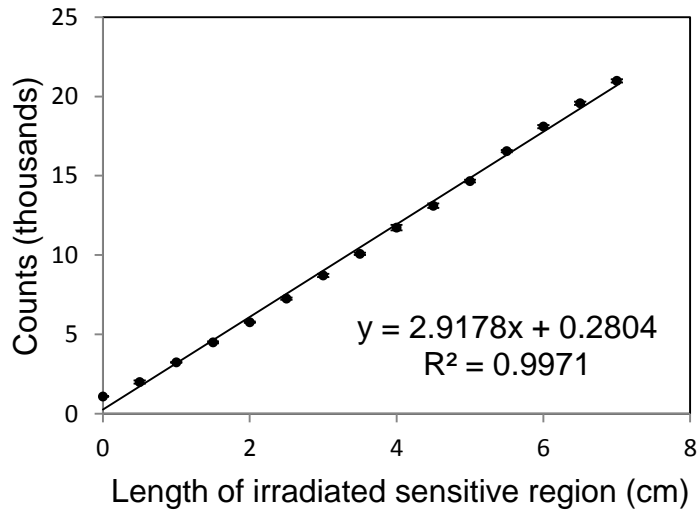


Figure 2-11. Spatial sensitivity of the 7cm FOC dosimeter. Linear fit was applied to the data along with a linear correlation coefficient. Error bars correspond to  $\pm 1$  standard deviation of the mean.

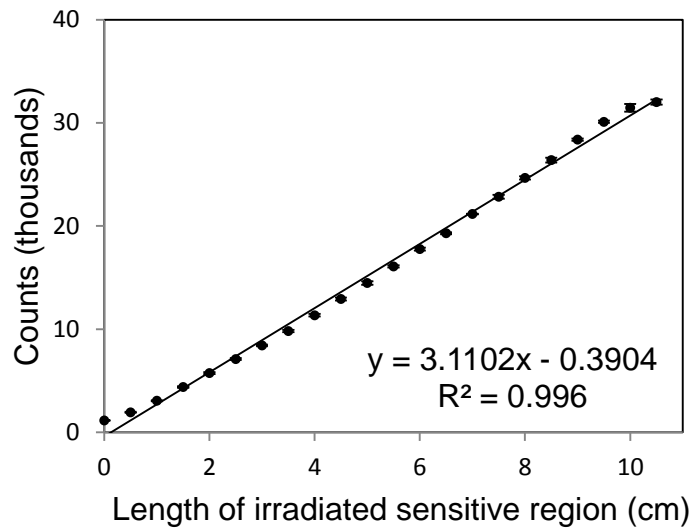


Figure 2-12. Spatial sensitivity of the 10cm FOC dosimeter. Linear fit was applied to the data along with a linear correlation coefficient. Error bars correspond to  $\pm 1$  standard deviation of the mean.

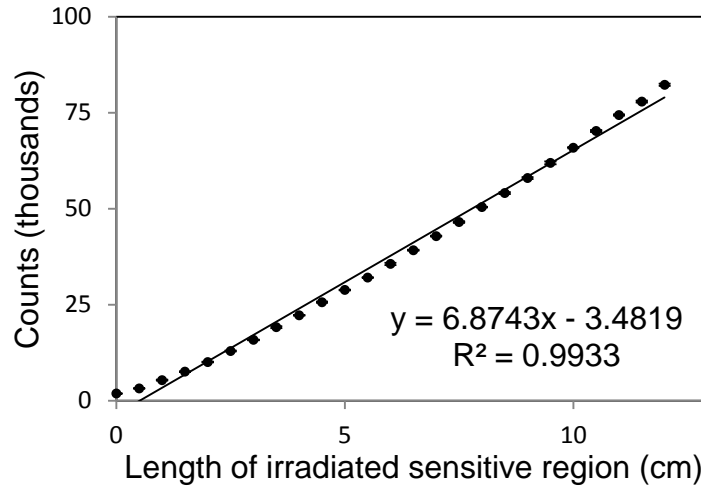


Figure 2-13. Spatial sensitivity of the 12cm FOC dosimeter. Linear fit was applied to the data along with a linear correlation coefficient. Error bars correspond to  $\pm 1$  standard deviation of the mean.

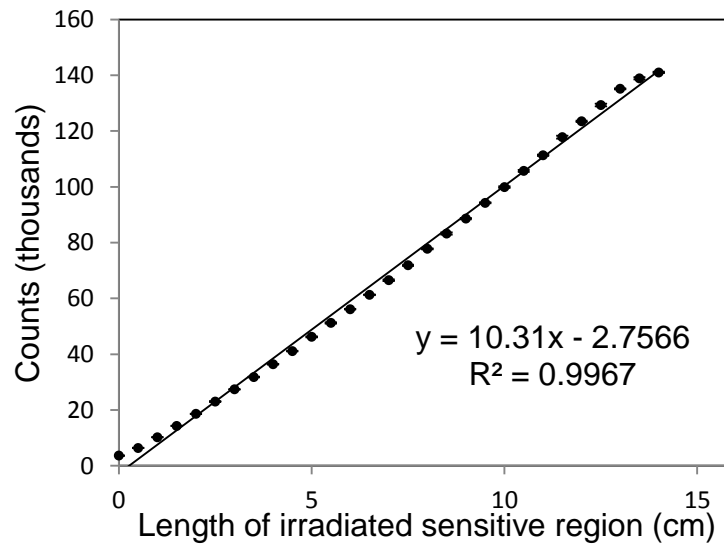


Figure 2-14. Spatial sensitivity of the 15cm FOC dosimeter. Linear fit was applied to the data along with a linear correlation coefficient. Error bars correspond to  $\pm 1$  standard deviation of the mean.

## CHAPTER 3 DEVELOPMENT OF A X-RAY/LIGHT FIELD CALIBRATION DEVICE

### **Introduction**

One key aspect of quality assurance in diagnostic imaging is the alignment between the x-ray field and light field. The light field is used to set up the patient for a particular study by providing a visual reference of the x-ray field size and location. The x-ray-to-light field alignment test ensures proper exposure of the patient, and imaging of anatomy critical for diagnosis.<sup>17</sup> It is the responsibility of the medical physicist to test and maintain congruence between the light and radiation fields in agreement with state and federal regulations. Traditional techniques to evaluate x-ray-to-light field misalignment focus around the use a combination of x-ray film or CR plates, and lead markers or coins, to define the boundaries of the x-ray and light field. This practice is quite satisfactory for physicists that have access to facilities or devices with film or CR processing capabilities. Digital systems, which now account for slightly over 80% of diagnostic mammography machines, do not use film and therefore might not have immediate access to film processing within the facility, unless a CR plate is used.<sup>18</sup> Similar methods capable of measuring the misalignment between the x-ray to light fields include the use of Gafchromic film.<sup>19</sup> This type of film does not require any post processing. However, the use of film can be quite cumbersome and susceptible to producing un-reliable measurements if not properly exposed. With Gafchromic film, the deviation between the two field edges is measured by optically placing a marker on the edge of the light field, and then using a ruler to measure the displacement between the marker and the edge of the darkened region on the film. Inaccuracies may result from the underexposure of the film. Additionally, each side of the image receptor, four sides

in total, must be evaluated leading to multiple exposures. In the case of digital mammography, multiple field sizes and locations may also be required to be tested, potentially resulting in up to 16 separate measurements.

To address these issues, a prototype detector was developed and characterized to streamline the overall process in evaluating the misalignment between the radiation and light fields. The detector was derived from the fiber-optic-coupled (FOC) dosimeter in Chapter 2.

### **Materials and Methods**

The FOC detectors were constructed using the same methodology in Chapter 2. The scintillating fibers however had length of 15mm, 20mm, 34mm, and 42mm to achieve a spatial domain for x-ray detection reasonable for x-ray/light field alignment. Each detector is capable of measuring one field edge. With four in total it would require an array of four PMT's to evaluate the entire field alignment.

The boundary of the radiation field is measured by placing a known length of the scintillating fiber into the light field. The signal intensity collected from an exposure correlates to the total volume of the scintillator irradiated. Since the diameter of the fiber is unvarying, the signal is proportional to the length of the fiber in the radiation field. Linearity of the detector with exposed length permits calibration to measure an absolute length of scintillation fiber exposed to the x-ray field. The x-ray to light field deviation may be determined from the known relative placement of the detector relative to the light field. The setup of this detection system is displayed in Figure 3-1. A series of experiments were conducted to characterize the spatial response of the scintillation fiber and to demonstrate that the detector exhibits a linear response with respect to exposed length.

## Results

After the detector assembly was constructed following the previously described methodology, it was tested to check for variability and linearity with respect to beam intensity. Readings were taken at discrete tube current settings, ranging from 12 to 200 mAs (time-current product), on an Instrumentarium Agfa IQ mammography imaging system. The edge of the scintillating fiber was optically aligned with the edge of the x-ray field which was determined using Gafchromic XR-CT film to ensure the scintillating fiber was completely exposed to the x-ray beam and the optical fiber was out of the radiation field. Figure 3-2 is a plot of the registered counts at different beam techniques of varying tube current, and a constant x-ray tube potential of 25 kVp.

The energy dependence of the detector was evaluated by incrementally increasing the tube potential from 20 kVp in steps of 2 kVp while maintaining the current-time product constant at 50 mAs. An ion chamber was placed adjacent to the FOC dosimeter and irradiated simultaneously to provide a measurement of air kerma from each exposure. The data, shown in Figure 3-3, describes the normalized detector sensitivity, in counts/mGy, versus tube potential.

Figure 3-4 is a plot of the detector's response to various exposures for sensitive element lengths of 3 mm and 42 mm. Exposures were taken at varying beam techniques by using different tube current and tube voltage settings. The two fibers were placed adjacent to one another at a position with relatively uniform spatial beam intensity. An ion chamber was also placed beside both of the fibers to provide a means for quantifying the air kerma at each exposure. The readings were normalized and plotted against the measurements from the ion chamber. This experiment offers a direct comparison of the detectors response to diagnostic energy x-ray beams. The 3-

mm detector serves as a benchmark, as it has been previously characterized as a diagnostic x-ray-detection instrument.

The final evaluation was to experimentally prove the spatial sensitivity of the detector would replicate the spatial sensitivity displayed by the linear FOC dosimeters in Chapter 2. Four detectors were evaluated, with sensitive element sizes of 1.5, 2.0, 3.4 and 4.2 centimeters. The detectors were irradiated using the mammography imaging system at two field edges, one perpendicular, the other parallel to the axis of anode-cathode axis. A step motor was used to incrementally insert each detector in and out of the x-ray field. The motor was placed perpendicular to the light field and inserted into the x-ray field. The results are displayed in Figure 3-5 and 3-6. One measurement was taken at each insertion step to mimic the calibration process, except in Figure 3-7, which used the mean of five measurements. Additional measurements lead to the coefficient of determination increasing from 0.997 to 0.999 for the 42-mm detector.

Figure 3-1 illustrates an example setup for a system monitoring digital x-ray field and light field alignment. Figure 3-8 describes the theoretical response of the detector and describes the two measurements needed to find the x-ray-to-light field misalignment. Each detector is marked with two lines to denote the calibration( $x'1$ ) and evaluation( $x'2$ ) locations. To evaluate all sides of the x-ray-to-light field alignment, four detectors are placed in the position so that the calibration marker on the detector is aligned with the light field boundary. At a specified beam technique, an exposure is delivered to the detectors. The reading is recorded and stored. The calibration reading is needed to determine the relative beam intensity of the detector. Afterwards, the detectors are moved to their field evaluation position, which is the evaluation marker on

the detector. The evaluation marker is placed so that it is aligned with the edge of the light field. The exposure is repeated at the same beam technique, and the reading is recorded. Using the calibration and evaluation reading, it is now possible to calculate the misalignment between the two fields using Equation 3-5. Equation 3-5 is derived from Figure 3-8, which shows the linear response of the sensitive element to exposed length. The light field is located at  $x'$  and distance  $a$  away from the location of x-ray field at position  $x$ .

The equation in slope-intercept form is written as:

$$y = mx + b = m(x' + a) + b = mx' + c \quad (3-1)$$

Substituting for  $m$ ,  $c$  can be expressed in terms of  $y_1$ ,  $x_2'$ ,  $\Delta y$ , and  $\Delta x'$ :

$$c = y_1 - \frac{y_2 - y_1}{x_2' - x_1'} * x_1' \quad (3-2)$$

Using Equation (3-1),  $c$  can also be expressed in terms of  $\Delta y$ ,  $\Delta x'$ , and  $b$ .

$$c = \frac{y_2 - y_1}{x_2' - x_1'} * a + b \quad (3-3)$$

The y-intercept,  $b$ , is a positive integer that accounts for the background signal collected by the detector when it is located outside the radiation field. It can be parameterized experimentally at different beam energies. Another method to find the y-intercept is to obtain a third measurement  $y_3$ , which represents the exposure when the detector is completely immersed in the radiation field. Using this measurement  $b$  can be determined using Equation 3-4.

$$b = y_3 - L * \frac{(y_2 - y_1)}{(x_2' - x_1')} \quad (3-4)$$

The solution for  $a$  can be expressed by combining Equation 3-1 and 3-3.

$$a = \frac{(y_1 - b)(x'_2 - x'_1)}{y_2 - y_1} - x'_1 \quad (3-5)$$

Equation 3-5 is the equation that calculates the deviation between the x-ray and light field at any beam technique. The measurement could be simplified by characterizing the fiber for  $m$  and  $b$  at a specific beam technique for the mammography system being evaluated.

$$a = \frac{y - b}{m} - x' \quad (3-6)$$

Using this method only one measurement would be required and the alignment could be readily determined. If one measurement is taken at  $x'$  and  $y$  counts are measured, the distance between the x-ray and light field could be quantified using Equation 3-6 by having a second detector fully in the beam.

## **Discussion**

### **Linearity, Reproducibility, and Energy Dependence**

The linear detector demonstrates an exceptional linear response with beam intensity and energy dependence within the range of the mammography imaging system tube potentials. When benchmarked against an ion chamber and the 3-mm detector, the 42-mm detector provided excellent reproducibility, and outperformed the 3-mm detector, with a coefficient of variation of 0.1% to 1.0%. This can be attributed to a higher signal to noise ratio resulting from a higher number of measured counts in the larger fiber.

The detectors demonstrated an overall linear response proportional to scintillating length irradiated. Non-linear effects occurred when the scintillator is not covered uniformly with the heat shrink wrap tubing resulting in varying beam intensity incident to

the scintillator due to effects of attenuation from the shrink wrap tubing. For example, an extra layer of heat shrink tubing (0.05 cm thick) will attenuate 5% of the all incident photons for mammography x rays. This is evident in the 3.4 cm and 2.0 cm detectors in Figure 3-5 and 3-6. The 1.5 cm and 4.2 cm detectors were constructed with uniform shrink wrap coverage. Another effect on the linear response of the fibers is the uniformity of the x-ray field. The x-ray field is relatively flat in every direction and was measured up to 20% difference between the edge of the x-ray field and a point 2 cm into the field. When evaluating an imaging system for x-ray-to-light field alignment it would be more accurate to minimize the size of the scintillating fiber. A general limit for mammography x-ray-to-light field alignment is that the device shall not exceed 2% of the source-to-image distance (SID).<sup>20</sup> A typical SID of 66 cm would require the alignment to be less than 1.32 cm in either direction. Taking that into account, the ideal scintillator would be between 3 and 3.5 centimeters for that particular unit.

### **Detector Resolution**

The detection resolution of the 42 mm detector was calculated using the slope from the exposed length response curve (Figure 3-7) and the standard deviation for the number of measured counts. Using these two values the system resolution, which is the equivalent to the full width at half maximum (FWHM) of the count distribution, can be expressed in Equation 3-7.

$$FWHM = 2.3\sigma_{mm} = 2.3 \frac{1}{m \left[ \frac{\text{counts}}{\text{mm}} \right]} \sigma_{counts} \quad (3-7)$$

The results of Equation 3-7 for the 42-mm detector show a maximum detector resolution within 0.38 mm and 0.29 mm for the 15-mm detector. The FWHM best

describes the distribution of measured counts at a specific insertion point. If the detector is moved slightly, the new distribution will overlap with the previous, resulting in uncertainty in the fibers actual position. Therefore by quantifying the FWHM, this uncertainty can be evaluated and expressed in terms of unit distance.

### **Conclusion**

Constructing an x-ray-to-light field alignment device using a fiber-optic detector system is practical in accurately evaluating the alignment between the two fields. It is also preferable to evaluate the x-ray-to-light field alignment at higher energies to minimize the effects of attenuation from the heat shrink tubing covering the fiber. Considerations should include scintillating fiber size, uniform encasing of shrink wrapping over scintillating fiber, and the field uniformity of the imaging system. When taking into account the variation in output, detection, and field size the device is capable of measuring a field alignment within 0.4 mm. This device is currently under patent, filed under patent number: UF #13472; Ref No. 222108-2160; PCT Application No. PCT/US11/44049; "Digital X-ray Field and Light Field Alignment.

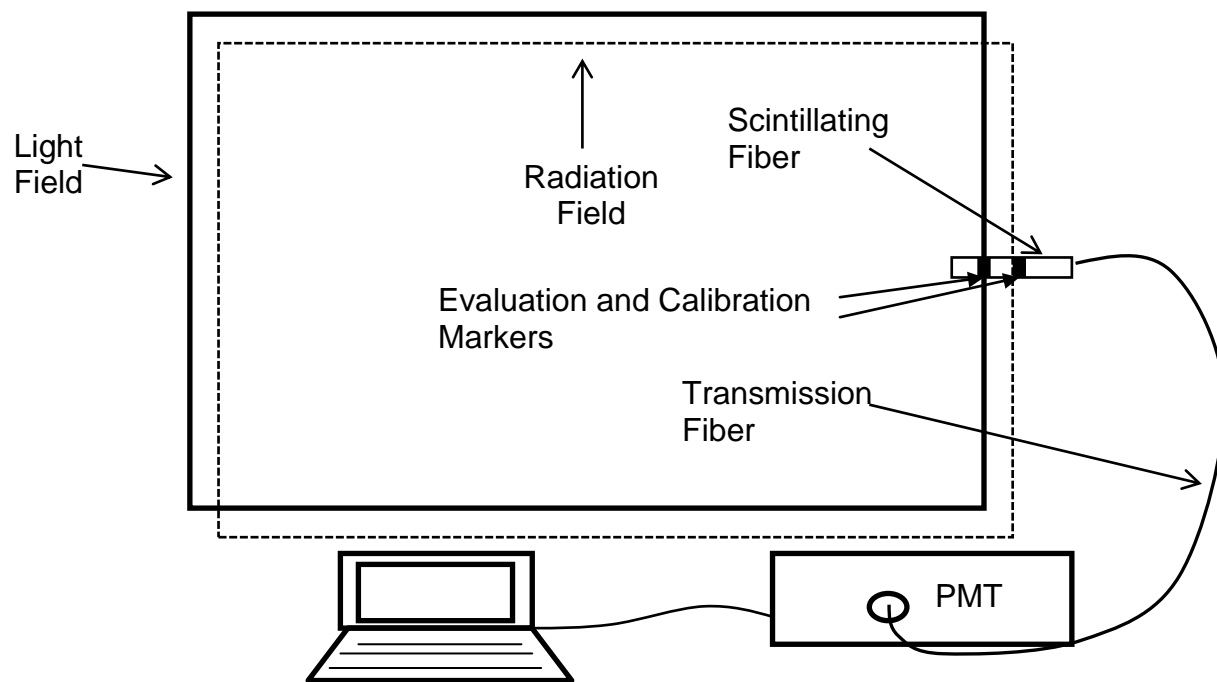


Figure 3-1. Schematic of x-ray-to-light field evaluation setup. Both the calibration and evaluation markers are shown on the detector.

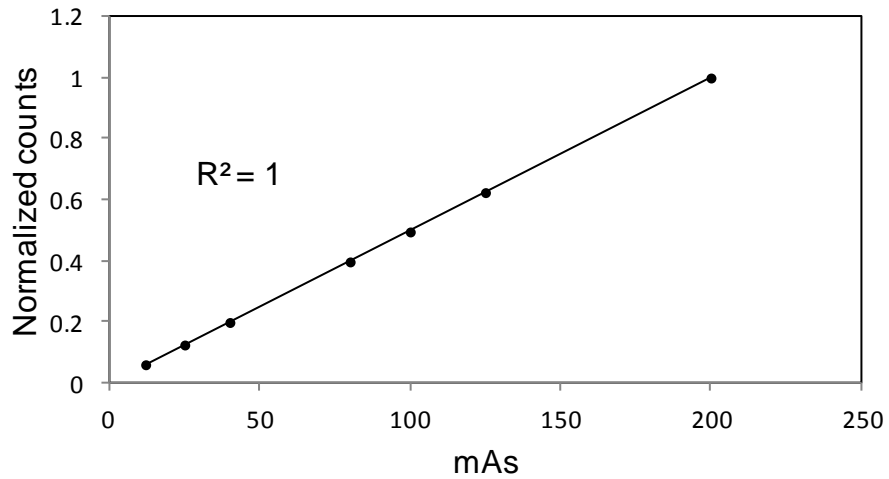


Figure 3-2. Plot of detector response to x-ray beam intensity, tube current-time product. Error bars are not shown because they are too small to be displayed. The measured counts were normalized to the maximum reading at 200 mAs. All exposures were delivered at 25 kVp.

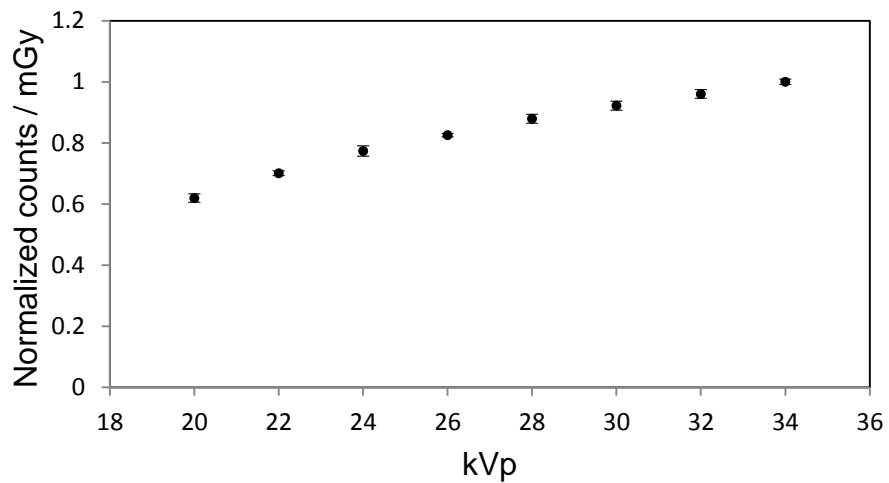


Figure 3-3. Detector's response to x-ray beam energy. Data has been normalized to the data point at 34 kVp. Error bars correspond to  $\pm 1$  standard deviation of the mean. The time-current product was consistently set at 40 mAs for all exposures.

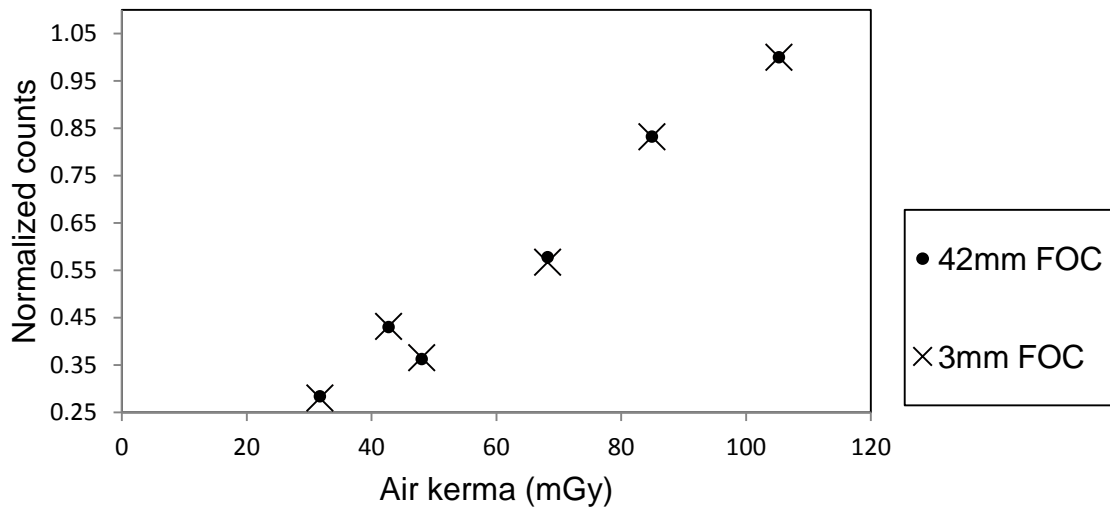


Figure 3-4. Response of the 3mm and 42mm FOC detectors to various beam intensities and energies. The data was normalized to the 100 mGy air kerma data point. Error bars are not shown because they are too small to be displayed.

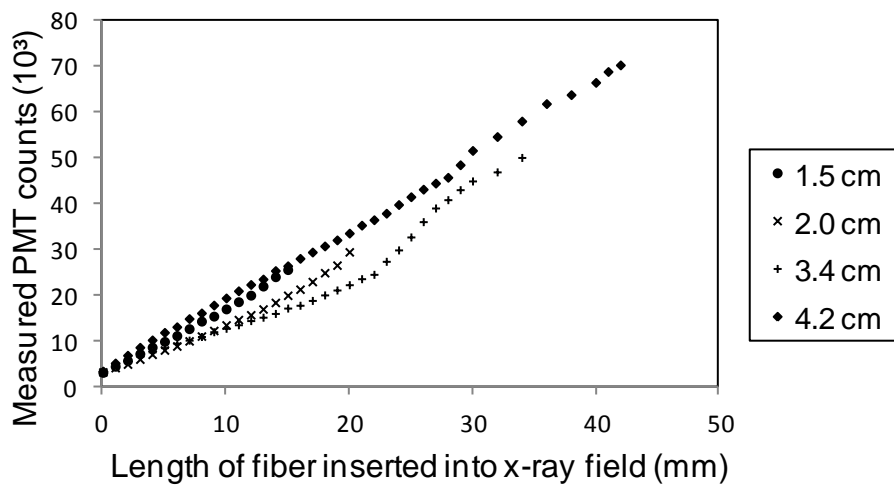


Figure 3-5. Detector spatial response to irradiation on x-ray field side perpendicular to the heel effect at 35 kVp and 40mAs. No error bars are shown because only one measurement was taken at each position.

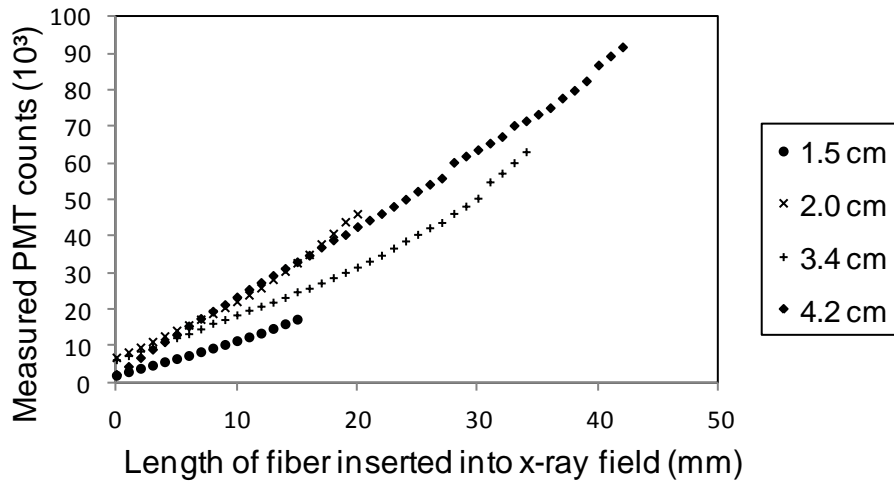


Figure 3-6. Detector spatial response to irradiation on x-ray field side parallel with heel effect at 35 kVp and 40mAs. No error bars are shown because only one measurement was taken at each position.

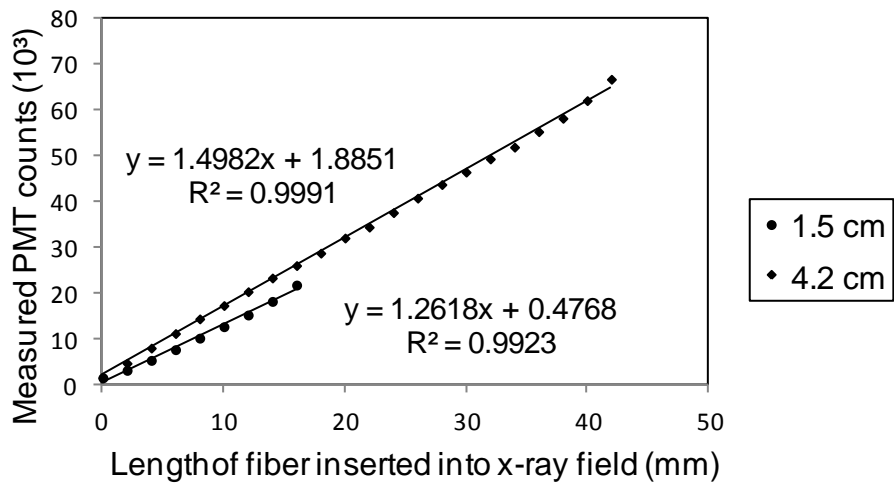


Figure 3-7. The 4.2 cm and 1.5 cm detector's response irradiated on x-ray field side perpendicular to the heel effect at 25 kVp and 40 mAs. The best fit curve is displayed for each fiber above (4.2 cm) and below (1.5 cm) their respective trend lines. Error bars were too small to be displayed, highest standard deviation of counts was 233 at 36mm insertion point for the 4.2 cm detector.

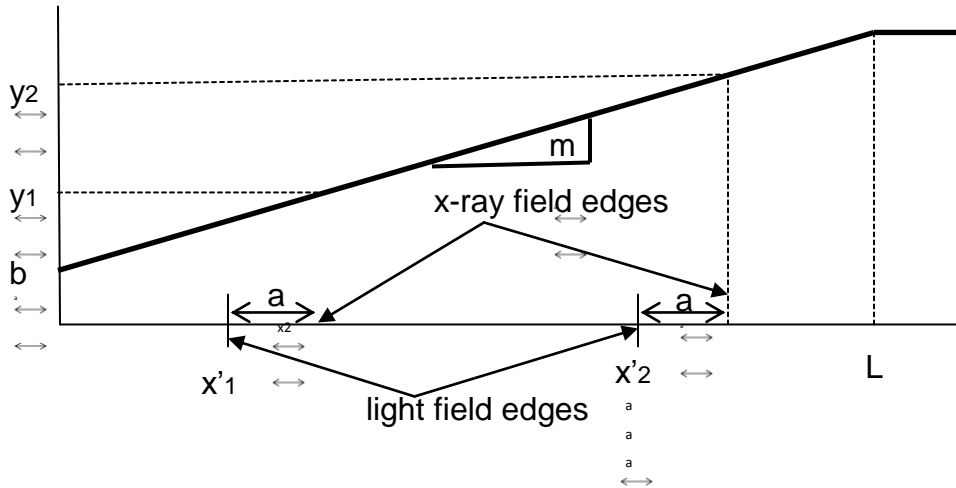
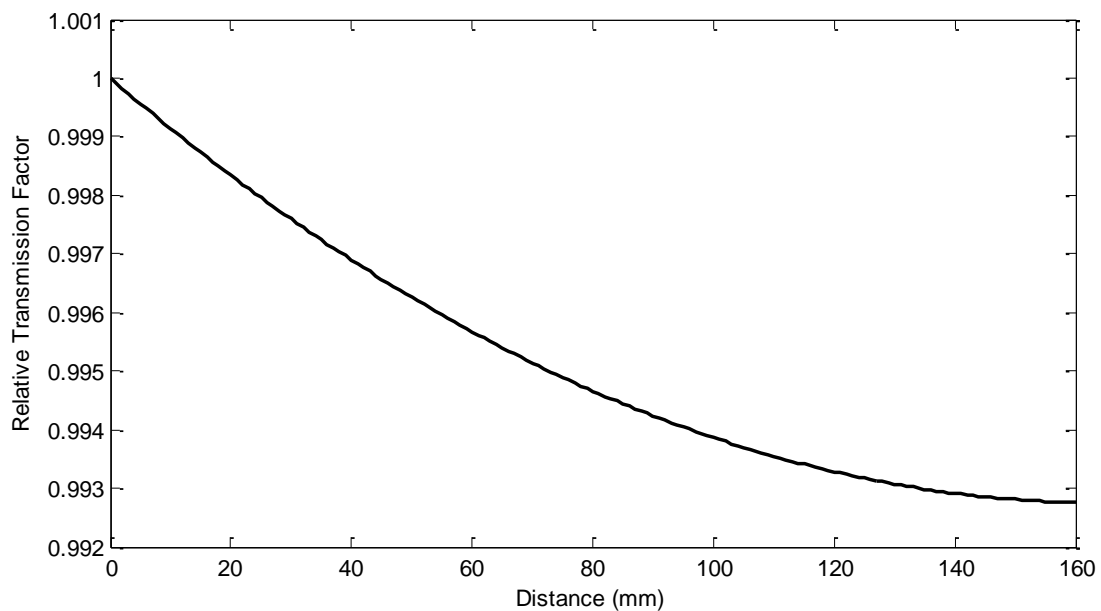


Figure 3-8. Plot of a detector's theoretical response to exposed length with measurements at points at  $(x'1, y1)$  and  $(x'2, y2)$  along with parameters  $m$  and  $b$  which characterize the response curve, and  $L$ , the length of the fiber.

APPENDIX A  
CODE FOR TABLE 1-1 & 1-2

```
%%%%%%%% Numerical Intergration of exponential attenuation in scintillating  
%%%%%%%% fiber  
  
theta=[-8.7/180*pi:0.001:8.7/180*pi()]; %range of acceptable angles  
  
N=length(theta);  
s=270; %attenuation coefficient  
L=4; % fiber length in cm  
  
%Initial Conditions  
x=0;  
i=1;  
  
f=zeros(160,1);  
for i=1:161  
    f(i)=1/2*trapz(exp(-x/s*sec(theta)))/N+1/2*0.95*trapz(exp(-(2*L-x)/s*sec(theta)))/N;  
    x=x+0.1;  
end  
  
x=[0:1:160];  
  
plot(x,f)
```



APPENDIX B  
CODE FOR FIGURE 1-4

```

%%%% Model of Geometric coupling efficiency of the optical fiber

D1=0.250; % diameter of the scintillating fiber
D2=0.200; % diameter of the optical fiber

L=400; %length of the fiber in mm
thetaa=8.7; %acceptance angle in degrees
int=D1-D2; % uncoupled width on the scintillator
%%%%%%%%%%%%%%%%%%%%%%%%%%%%%%%%%%%%%%%%%%%%%%%%%%%%%%%%%%%%%%%%%%%%%%%%
s1=4*tan(thetaa*pi/180)*L;
a=s1/D1; % not accounting for the initial matrix
b=a-fix(a); % left over fraction of D1
c=round((b*D1/0.005)/2); % number of intervals on each side

n=zeros(1,c);

for i=1:c

    if (i <= 5)
        n(i)=0;
    else
        n(i)=1;
    end

end

nflip=flipr(n);

n1=zeros(1,5);
n2=ones(1,40);
n22=ones(1,20);

n3=[n1 n2 n1];

n4= repmat(n3,1,fix(a/2)+1);

nbig=[nflip n4 n1 n22 1 n22 n1 n4 n]; %biggest possible matrix

centerpoint=length(nflip)+length(n4)+1+length(n1)+length(n22); %center value for r=0
in nbig

%%%%%%%%%%%%%%%%%%%%%%%%%%%%%%%%%%%%%%%%%%%%%%%%%%%%%%%%%%%%%%%%%%%%%%%%

fx=zeros(1,401);

```

```

for i=1:401

    j=i-1;

    width=round(2*tan(thetaa/180*pi)*j/0.005); %number of pixels

    width2=round(2*tan(thetaa/180*pi)*(2*L-j/L)/0.005); %number of pixels

    fr=zeros(1,51);
    fr2=zeros(1,51);

    for k=1:51
        fr(k)=mean(nbig((centerpoint+(k-1)-fix(width/2)):(centerpoint+fix(width/2)+(k-1))));
    end

    for l=1:51
        fr2(l)=mean(nbig((centerpoint+(l-1)-fix(width2/2)):(centerpoint+fix(width2/2)+(l-1))));
    end

    for m=2:51

        fr(m)=fr(m)*(m-1)*2*pi; %weighted based on size
        fr2(m)=fr2(m)*(m-1)*2*pi; %weighted based on size
    end

    fyy=cumsum(fr)/(pi*50^2);
    fyyy=cumsum(fr2)/(pi*50^2);

    fx(i)=(fyy(51)+fyyy(51))/2;

end

x=[0:0.01:4];
plot(x,fx)

```

## LIST OF REFERENCES

1. L. Archambault, J. Arsenault, J. Gingras, A. S. Beddar and L. Beaulieu, "Plastic scintillation dosimetry: Optimal selection of scintillating fibers and scintillators," *Med Phys* **32**, 2271-2278 (2005).
2. J. Meyerott, P. C. Fisher and D. T. Roethig, "Plastic scintillator response to 1-10 keV photons," *Rev Sci Instrum* **35**, 669-672 (1964).
3. F. H. Attix, *Introduction to Radiological Physics and Radiation Dosimetry*. (Wiley-VCH, Hoboken, NJ, 1986).
4. K. Jones, D.E. Hintenlang, "Potential clinical utility of a fiber-optic coupled dosimeter for dose measurements in radiology," *Radiat Prot Dosimetry* **132**, 80-87 (2008).
5. D. E. Hyer, R. F. Fisher and D. E. Hintenlang, "Characterization of a water-equivalent fiber-optic coupled dosimeter for use in diagnostic radiology," *Med Phys* (2009).
6. J. F. Winslow, D. E. Hyer, R. F. Fisher, C. J. Tien and D. E. Hintenlang, "Construction of anthropomorphic phantoms for use in dosimetry studies," *J App Clin Med Phys* **10**, 195-204 (2009).
7. ICRP, "Recommendations of the International Commission on Radiological Protection, Publication 26," *Vol. 26*, (The International Commission on Radiological Protection, New York, 1977).
8. ICRP, "Recommendations of the International Commission on Radiological Protection, Publication 60," *Vol. 30*, (The International Commission on Radiological Protection, New York, 1991).
9. A.S. Beddar, S. Law, N. Suchowerska and T. R. Mackie, "Plastic scintillation dosimetry: Optimization of light collection efficiency," *Phys Med Biol* **48**, 1141-1152 (2003).
10. Saint-Gobain Ceramics and Plastics Inc, "Scintillation BCF-12 material data sheet," (Saint-Gobain Crystals, Inc, Hiram, OH, 2008).
11. Polymicro Technologies, "Specification Sheet: FVP400440480," (Phoenix, AZ, 2008).
12. M. Kuhlen, M. Moszynski, R. Stroynowski, E. Wicklund, B. Milliken, "Timing properties of long scintillation counters based on scintillating fibers," *Nuclear Instruments and Methods in Physics* **301**, 223-229 (1991).
13. C.J. Tien, Ph.D. thesis, University of Florida, 2011

14. D.E. Hyer, Ph.D. thesis, University of Florida, 2010
15. A.S. Beddar, T. R. Mackie and F. H. Attix, "Cerenkov light generated in optical fibers and other light pipes irradiated by electron beams," *Phys Med Biol* **37**, 925-935 (1992).
16. Hamamatsu Corporation, "Specification Sheet: E5776-51," (Hamamatsu Corporation, Bridgewater, NJ, 1994).
17. AAPM Diagnostic X-ray Imaging Committee Task Group #12, "AAPM Report No. 74: Quality control in diagnostic radiology," (American Association of Physicists in Medicine, College Park, MD, 2008).
18. U.S. Food and Drug Administration, "Mammography Quality Standards Act Program National Statistics," (US D. o. Health, Silver Spring, MD, 2012).
19. Advanced Materials, "Collimation Assessment using Gafchromic XP-M," (International Specialty Products, Waynes, NJ, 2008).
20. Florida Department of Health, "Chapter 64E-5, Florida Administrative Code, X-Ray in the healing arts," edited by FL. D. o. Health (Tallahassee, FL, 2007).

## BIOGRAPHICAL SKETCH

Matthew Robert Hoerner was born in Pittsburgh, Pennsylvania to Karen Flory and Richard Hoerner. He is one of two children, along with his younger brother Michael. He graduated from Unionville High School in Kennett Square, Pennsylvania in 2005. Four years later he graduated from The Pennsylvania State University with a Bachelor of Science in Engineering degree in nuclear engineering. In 2009, Matthew enrolled into the medical physics graduate program at the University of Florida where he completed his master's degree in 2012. Matthew is committed to continuing his research at The University of Florida to pursue a doctorate in biomedical engineering.